Multiple Frequency Electron Cyclotron Heating for the Levitated Dipole Experiment

by

Scott B. Mahar

Submitted to the Department of Nuclear Science and Engineering
in partial fulfillment of the requirements for the degrees of

Master of Science in Nuclear Science and Engineering

and

Bachelor of Science in Nuclear Science and Engineering

at the

MASSACHUSETTS INSTITUTE OF TECHNOLOGY

(June 2005)
May 2005

MASSACHUSETTS INSTITUTE OF TECHNOLOGY
MAR 2 8 2006
LIBRARIES

© Massachusetts Institute of Technology 2005. All rights reserved.

ARCHIVES

Author ....
Department of Nuclear Science and Engineering
May 20, 2005

Certified by ....
Jay Kesner
Senior Scientist
Thesis Supervisor

Read by ....
Ronald Parker
Professor, Elec Eng-Comp Sci, Nuclear Eng
Thesis Reader

Accepted by ....
Jeffrey Coderre
Associate Professor of Nuclear Science and Engineering
Chairman, Department Committee on Graduate Students

Multiple Frequency Electron Cyclotron Heating for the Levitated Dipole Experiment

by

Scott B. Mahar

Submitted to the Department of Nuclear Science and Engineering
on May 20, 2005, in partial fulfillment of the
requirements for the degrees of
Master of Science in Nuclear Science and Engineering
and
Bachelor of Science in Nuclear Science and Engineering

Abstract

The use of multiple frequencies of electron cyclotron resonance heating (ECRH) in the Levitated Dipole Experiment (LDX) is an important tool that will tailor the plasma profiles. Initial LDX plasmas have been created using 2.45 GHz and 6.4 GHz, both at up to 3 kW. The construction and calibration of the ECRH system will be discussed and initial experimental results will be presented. The effects of different combinations of pulse lengths and powers will be examined in terms of the plasma diamagnetism. Different density profiles will be used to calculate the locations of the resonances and cutoffs. Locations where the plasma absorbs the microwave power will be simulated through computer codes. Equilibrium output of the program DIPOLEQ combined with MATLAB calculations using the Appleton-Hartree dispersion relation provide qualitative representations of where the power is absorbed in typical LDX plasmas.

Thesis Supervisor: Jay Kesner
Title: Senior Scientist

Acknowledgments

I would like to thank my research advisors, Alex Hansen, Jay Kesner, and Darren Garnier for their help and guidance with this thesis. They have always been available to answer questions and offer insight into not only the problems at hand, but also plasma physics in general. I also would like to thank my thesis reader, Ronald Parker, for reviewing this thesis.

I am very grateful to the other members of the LDX group, without everyone working together LDX would not be where it is today. I would like to thank my fellow graduate students, Ishtak Karim, Eugenio Ortiz, Jennifer Ellsworth, Alex Boxer, and Austin Roach. I thank Mike Mauel for his leadership in the project as well as Alex Zhukovsky and Joe Minervini for developing and maintaining our superconducting coils. I also thank our technicians, Rick Lations and Don Strahan, as well as Edward Fitzgerald and Tom Toland for their help with the 2.45 GHz feed-through.

Finally I would like to thank my friends and my family, Jan, Mike, and Heather Mahar, for their support throughout my life.

Contents

1 Introduction **15**

1.1 Background 15

1.2 Outline 19

2 Overview of the Levitated Dipole Experiment **21**

2.1 Magnetic Geometry 21

2.2 Diagnostic Overview 24

2.3 Typical Plasma Shot 26

3 ECRH Heating Systems **31**

3.1 Hardware 31

3.1.1 2.45 GHz System 31

3.1.2 6.4 GHz System 35

3.2 Triggering 38

3.3 Data Acquisition 40

3.4 Calibration 41

3.5 Typical Plasma Shot 44

4 Plasma Resonances and Cutoffs **51**

4.1 Cold Plasma Dispersion Relation 51

4.1.1 Resonances 52

4.1.2 Cutoffs 53

4.1.3 Effect of Density on Resonances and Cutoffs 54

5 Power Absorbed Calculations 61

5.1 Average Power 62

5.2 Stix's Approximation 67

6 Conclusion 73

List of Figures

1-1 Dipole magnetic field confinement of the plasma surrounding Jupiter (J Spencer). 16

2-1 Cross section of the Levitated Dipole Experiment. 22

2-2 Photograph inside LDX vacuum vessel (left) and computer simulation of magnetic flux lines and resonances (right). 24

2-3 Initial diagnostic set of the Levitated Dipole Experiment. 25

2-4 Top and side views of the plasma heated by 6.4 GHz only (left), 2.45 GHz only (middle), and both sources (right). 26

2-5 Magnetic geometry when the coil is levitated without any current in the Helmholtz coils (left) and with 80 kA in the Helmholtz coils (right). 27

2-6 The fundamental resonances for F-Coil currents of 750 kA turns, 888 kA turns, and 1186 kA turns. The computer simulations for the rest of this thesis use an F-Coil current of 888 kA turns. 28

2-7 Different magnetic geometries for plasmas with the F-Coil levitated. . 29

3-1 2.45 GHz system. 32

3-2 2.45 GHz directional coupler with the DC block, attenuator, and detector diode attached. 33

3-3 2.45 GHz waveguide section with the window inside. 34

3-4 Diagram of a waveguide cut at the Vlasov angle. 34

3-5 2.45 GHz antenna and conflat. 35

3-6 6.4 GHz system. 35

3-7 6.4 GHz klystron. 36

3-8 6.4 GHz window. 37
3-9 6.4 GHz antenna and conflat. 38
3-10 Triggering system including the fiber optic converter and switch. . . . 39
3-11 DC block, 10 dB attenuator, and Zero Bias Schottky Detector Diode. 40
3-12 Calibration plots of signal voltage versus power. 43
3-13 Calibration plots of source dial setting versus power. 44
3-14 Fundamental and first harmonic resonances for both sources. 45
3-15 Picture of plasma formed by the 2.45 GHz source (left). Same picture with the fundamental and first harmonic resonances superimposed (right). (shot: 50317015) 46
3-16 Data from a modulation shot where the 6.4 GHz source was on from 0 to 8 seconds and the 2.45 GHz source was turned on and off. 47
3-17 Comparison of diamagnetism from the 2.45 GHz (shot: 50318001 in gray) and 6.4 GHz (shot: 50317012 in black) sources. 48
3-18 Comparison of diamagnetism from the 2.45 GHz and 6.4 GHz sources during a modulation shot. In shot 50318009 (black) the 6.4 GHz system is modulated, and in shot 50318007 (gray) the 2.45 GHz system is modulated 48
3-19 Data from a shot showing the low density (0-0.25 sec), high density (0.25 sec - 4 sec), and afterglow (after 4 sec) regimes. 49

4-1 Upper hybrid resonances for both frequencies. 54
4-2 Density cutoffs. 55
4-3 Right Hand Cutoffs for both frequencies. 56
4-4 Possible density profiles. 57
4-5 Plasma frequency profiles for several density profiles. 58
4-6 High density cutoffs for several density profiles. 59
4-7 Right hand cutoffs for several density profiles. 60

5-1 Pressure, density, and temperature profiles for $n = C\psi^{\alpha}$. 64
5-2 Power absorption for a profile where $\alpha = 1$, $(n = C\psi)$. 66

5-3 Power absorbed (per unit area) calculations using Stix's approximation before being normalized. 68

5-4 Power absorbed per flux loop (left) and vs major radius (right) for $n = C\psi^{\alpha}$ calculated using Stix's approximation. Data is plotted for $\alpha = 0$, $\alpha = 1$, and $\alpha = 2$. 70

5-5 $\frac{d(Power)}{d(Volume)}$ plotted vs. $X(m)$ calculated using Stix's approximation. Data is plotted for $\alpha = 1$ $(n = C\psi)$. 71

5-6 Locations of flux loops with maximum absorption for $\alpha = 1$, $(n = C\psi)$. 72

List of Tables

2.1 Plasma Parameters for different optimizations with the F-Coil levitated. Column A is for a plasma that is diverted but is not shaped by the Helmholtz coils. Column B is for a diverted plasma with the Helmholtz Coils at values which maximize beta. Column C is similar to B except the Helmholtz coils are at values to minimize beta. 29

Chapter 1

Introduction

1.1 Background

The Levitated Dipole Experiment (LDX) uses electron cyclotron resonance heating (ECRH) to create and heat the plasma. Electrons in the initial plasmas are heated to temperatures on the order of tens of keVs up to 100 keV. These initial plasmas are heated using two sources of different frequencies in order to heat different areas of the plasma. By depositing power in different areas of the plasma, the pressure profile of LDX can be modified.

The goal of LDX is to study the stability and confinement of high beta plasmas. A dipole magnetic field provides the magnetic confinement for the plasma, while the plasma's compressibility provides the stability [1]. The dipole magnetic field is the simplest magnetic field, and is used as the confining field in LDX. Similarly, magnetized planets have a magnetosphere which can be approximated as a simple dipole magnetic field [2]. Akira Hasegawa first considered using a levitated dipole to confine hot plasma for fusion power after his participation with Voyager II [1]. The dipole magnetic field around Jupiter confines a plasma as shown in figure 1-1. The confinement using a levitated dipole's magnetic field has several advantages over the conventional tokamak confinement, making LDX attractive for fusion reactor research.

One of the biggest problems facing the tokamak fusion community is making

Figure 1-1: Dipole magnetic field confinement of the plasma surrounding Jupiter (J Spencer).

a reactor that is steady state. The operation of a levitated dipole fusion reactor would be relatively steady state, lasting as long as the floating coil could remain superconducting. Although this would not be technically steady state, progress in high temperature superconductors will allow the operation to proceed uninterrupted for at least hours, if not days. Utilization of an internal refrigerator could make such a device truly steady state [4].

Another advantage of a fusion reactor like LDX is that it is magnetohydrodynamically stable [3]. LDX has only poloidal field lines with no magnetic shear. This lack of magnetic shear predicts that the particle and energy confinement are decoupled [12]. Having only a poloidal field gets rid of particle drift from flux surfaces, and other neoclassical effects. The stability of LDX comes from the compressibility of the plasma. For example, the compressibility stabilizes the interchange mode when the pressure profile satisfies the adiabaticity condition: $\Delta(pV)^{\gamma} = 0$ where $V = \int \frac{dl}{B}$ is the flux tube volume and $\gamma = \frac{5}{3}$ is the ratio of specific heats [5]. Similarly, plasmas satisfying the adiabaticity condition are also stable to ballooning modes [6]. For equilibria with marginal profiles with $\eta = \frac{dlnT}{dlnn} = \frac{2}{3}$, drift waves are also stable [7].

The first plasmas in LDX were in supported mode: the "floating" coil was held in place by three supports. This permitted losses of particles where the field lines intersect the supports, as well as particles on these field lines that pitch angle scatter. However, in levitated mode, these supports will not be present and all plasma losses will be radial, across the field lines. The dipole field lines will form closed loops, in a toroidal configuration.

One consequence of a levitated coil is that it limits the mass that can be devoted to shielding. Without heavy shielding, high energy 14 MeV neutrons from D-T fusion would penetrate and heat the coil. Therefore, an LDX reactor will have to use D-D and D-He^3 reactions, which will increase the confinement needed to produce the same fusion reaction rate [8] [4].

There are three superconducting magnets used in LDX. A 550 kg Nb3Sn superconducting floating magnet, carrying a current up to 1.2 MA, makes the dipole magnetic field [9]. In order to charge the floating magnet inductively, a super conducting charging magnet is used. Since the dipole magnet must be floating to produce a dipole magnetic field without end losses, a levitation coil is needed to provide the magnetic force to levitate the floating coil. Additionally, Helmholtz coils are positioned to provide a vertical field in order to form a separatrix in the plasma when the coil is supported, as well as for general shaping of the plasma.

In order to heat the plasma to substantial pressure and beta values, LDX uses multiple frequency electron cyclotron heating. Two sources, 2.45 GHz and 6.4 GHz, currently heat the plasma, and future plans include sources at 10.5 GHz, 18 GHz, and 28 GHz. The current sources operate at 3 kW each; however, the future sources will have higher power, such as the 10.5 GHz with 10 kW. Combinations of different source fire times and different power levels will be used to study different plasma pressure profiles [10].

For the initial plasma runs, only limited diagnostics are available. These include several flux loops, Mirnov coils, an interferometer, four chords of an x-ray pulse height analyzer, an NaI scintillation detector, a photodiode, and several probes including a

Mach probe, a triple probe, and swept Langmuir probes.

Heating is necessary to produce plasma that is physically interesting to study. The use of multiple frequency electron cyclotron heating in magnetic mirror experiments demonstrated a reduction in plasma turbulence as well as an increase in the plasma heating efficiency [5]. Since LDX currently uses two frequencies to heat the plasma, there are many combinations of powers and time sequencing among the two sources that can be studied. The addition of more sources will introduce many more variables that will aid in the control of the plasma.

In the Collisionless Terrella Experiment (CTX) at Columbia University electron cyclotron resonance heating has been studied in the presence of structural end losses. From this research it is believed that when the dipole is levitated and there are no structural end losses, high beta plasmas should be able to be produced from a few tens of kW of microwave power [1].

One of the major benefits of using multiple frequency electron cyclotron heating is that different combinations of power levels in each of the frequencies can be used to shape the plasma [10]. Each frequency has a unique zone of resonant interaction where the microwave power is absorbed [11]. Using data from the x-ray pulse height analyzer, which measures the energy spectrum of the x-rays emitted from the hot electron Bremsstrahlung radiation, the temperature of the electrons can be calculated [12]. According to ideal MHD, marginal stability for interchange modes results when the pressure profile satisfies the adiabaticity condition [5]. Since the most important MHD instabilities are pressure driven, being able to calculate and define the pressure profile is very advantageous in researching the high beta plasmas that will be created in LDX.

The most important resonances for both sources currently in use in heating the LDX plasmas are the fundamental and first harmonic electron cyclotron resonances. These resonances are regions of constant magnetic field magnitude, which cut across the magnetic field lines. Since each magnetic field line intersects each resonance, there is potential for power absorption at each frequency on each magnetic field line; however, the power absorbed depends on many more factors. For example, regions where the magnetic field lines are tangent to the resonance, normally on the midplane, will experience more power absorption since the electrons will be in the area of resonance for a longer time. Other factors that contribute to the power absorption function are the local density and the direction of propagation of the heating wave.

Both the 2.45 GHz source and the 6.4 GHz source are launched nominally in X-mode at a side port on the vacuum vessel with antennas cut at the Vlasov angle in order to minimize the reflected power and to minimize the directivity. The intended heating scheme for LDX uses "cavity heating", which assumes a small first-pass absorption and many reflections off of the vacuum walls to make the heating as isotropic as possible [7]. The 10.5 GHz system will be launched from the bottom of the vessel up toward the center of the floating coil.

Since LDX heats the electrons, the right hand cutoff is the most important cutoff for the propagating waves. Using the cold plasma dispersion relation, the location of the right hand cutoff can be found and plotted. Another important cutoff that comes from the dispersion relation is the density cutoff. This is the point in the plasma where the density is high enough to make the plasma frequency larger than the frequency of the input heating wave, causing it to evanesce. Since LDX only has a calculation of the pressure profile, as well as point measurements of the edge density and a single chord for the line-averaged density, the exact density profile is not known. Several potential density profiles have been suggested; however, the locations of these cutoffs vary significantly depending on what density profile is chosen. Chapter Four will go into more detail about the relative positions of the cutoffs and the resonances as a function of density.

1.2 Outline

The purpose of this thesis is to discuss the setup and calibration of the 2.45 GHz and 6.4 GHz systems and to make some general calculations involving the cutoffs and resonances for typical plasma shots.

Chapter Two gives an overview of LDX, including the geometry of the experiment, the initial diagnostics, and data from typical plasma shots. The Third chapter goes into more detail with respect to the hardware, data acquisition, and calibrations of both systems. Chapter Four focuses on the resonances and cutoffs in a typical LDX plasma. Since there is no definite measurement of the density profile, several different profiles are examined, along with the profile's effects on the resonances and cutoffs. A calculation of the power absorbed by the plasma in different zones of the plasma is presented in Chapter Five. The final chapter includes conclusions and a brief overview of future ECRH work for LDX.

Chapter 2

Overview of the Levitated Dipole Experiment

The Levitated Dipole Experiment is designed to study plasma confinement in plasma confined by a dipole magnetic field. Akira Hasegawa was the first person to suggest the use of a dipole magnetic field to confine plasma after his participation with Voyager II. Fluctuations in laboratory plasmas often lead to rapid plasma and energy loss; however, fluctuations in planetary magnetospheres lead to inward diffusion and heating [2]. This discovery prompted the development of many different plasma confinement research projects. The Collisionless Terrella Experiment (CTX) is an experiment at Columbia University that studies the physics of plasma confined by a supported dipole [15]. Although CTX is much smaller than LDX when the F-coil is supported, a lot of the plasma physics is the same. Another experiment similar to LDX is the Levitated Superconducting Ring Trap (Mini-RT) in Japan. This experiment has a 6 cm diameter levitating magnet which produces a dipole field, and the physics of its single species cold plasma is studied [16].

2.1 Magnetic Geometry

The major difference between LDX and CTX is that the F-coil that produces the dipole field in LDX will eventually be floating during operation. Currently, LDX

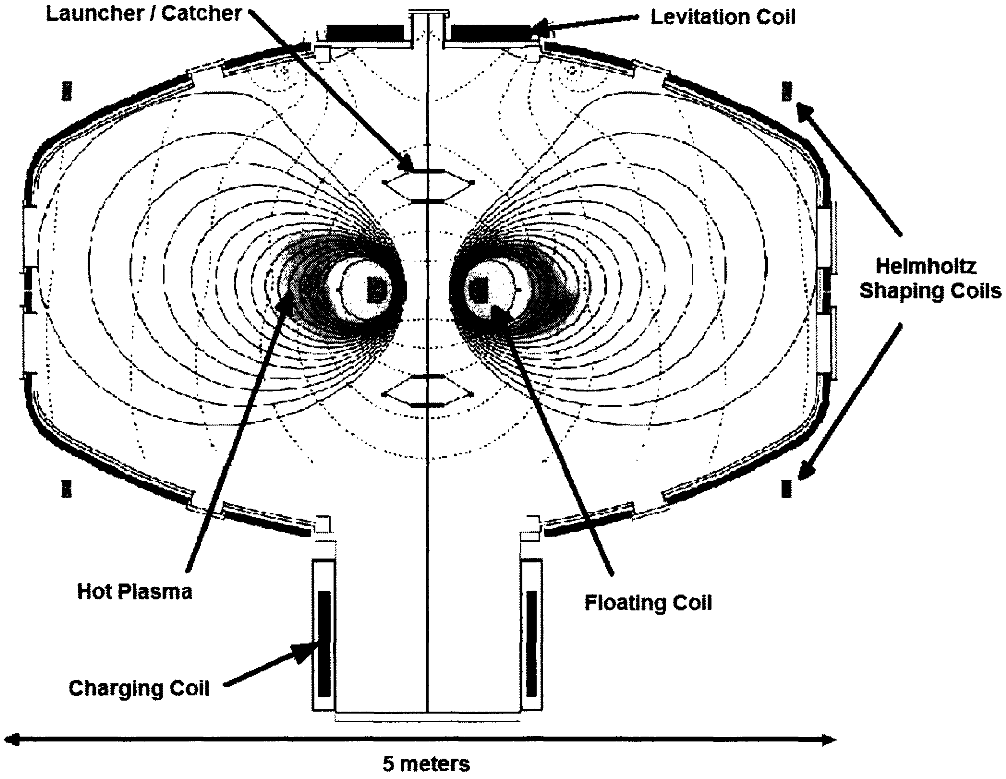

Figure 2-1: Cross section of the Levitated Dipole Experiment.

operates in supported mode: the F-coil is not floating but rather is mechanically supported in its position. The support structure allows end losses, since some of the magnetic field lines run into the supports. Although this enhances plasma losses, it does not affect the magnetic geometry of LDX.

The Levitated Dipole Experiment utilizes several important superconducting magnets shown in figure 2-1. The Floating Coil (F-Coil) is the 64 cm diameter magnet that creates the dipole magnetic field. Composed of Nb3Sn, the F-Coil must be cooled down to 4 degrees Kelvin to become superconducting. The 550 kg coil can carry a maximum of 1.2 MA of current and can remain superconducting for approximately 2.5 hours [17]. Since the F-coil floats in the middle of the hot electron plasma, its design is very complicated due to many constraints. Enough shielding must be used to protect the superconducting magnet from radiation, an internal liquid helium "refrigerator" must keep the coil at 4 degrees Kelvin, and the coil must be relatively light so it is possible for it to be levitated by another magnet.

Since the F-coil does not have any leads, it needs to be inductively charged. The Charging Coil (C-coil) is also a superconducting magnet; however, this magnet is made out of NbTi. To maintain its superconductivity, it must be cooled to 4.5 degrees Kelvin, and it can create a peak field of 4.3 Tesla [17]. The F-coil fits inside the 1.2 m bore of the C-coil, where it is inductively charged and cooled to make it superconducting and freeze in the magnetic flux.

In order to have closed magnetic field lines, the F-Coil must be levitated. The Levitation Coil (L-Coil) is positioned on the top of the vacuum vessel. This coil will attract the F-Coil and allow it to float at the center of the vacuum vessel. An active feedback system will monitor the position of the F-Coil and adjust the current in the L-Coil accordingly. The L-Coil is the first high temperature superconducting coil used in the fusion community. It is made out of BSSCO-2223 conductor and is superconducting up to temperatures around 77 degrees Kelvin, although its operating temperature will be 20-25 degrees Kelvin [17].

Another set of coils used on LDX are the Helmholtz Shaping Coils. These coils have a diameter of approximately 5 m and are positioned above and below the vacuum vessel to create a vertical field. The Helmholtz coils are made of copper, wound in four layers of four windings. The purpose of these coils is to form and control the position of a separatrix in the plasma. In doing this, the coils can change the compression ratio as well as the marginal stable pressure profile [17].

Having several different coil systems allows LDX to be able to modify the magnetic geometry inside the vacuum vessel. By varying the magnetic geometry and pressure profile, many physics experiments can be performed to learn more about plasma confinement in the dipole geometry.

During a shot without the Helmholtz Coils, the magnetic geometry looks similar to figure 2-2. The left side is a photograph inside the vacuum vessel, and the right side shows the magnetic field lines, the surfaces of constant magnetic field magnitude, and location of the resonance zones. Also, the location of the 2.45 GHz and 6.4 GHz waveguide antennas can be seen on the right side.

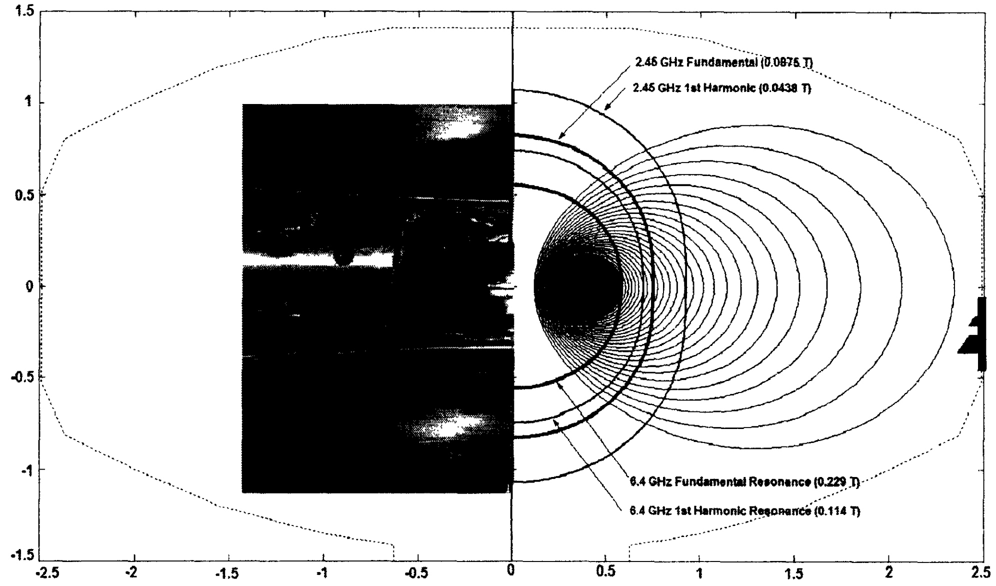

Figure 2-2: Photograph inside LDX vacuum vessel (left) and computer simulation of magnetic flux lines and resonances (right).

2.2 Diagnostic Overview

The most important measurements of fusion plasmas are the density and temperature profiles. For the initial plasma runs, only limited diagnostics are available. These diagnostics, shown in figure 2-3, include several flux loops, Mirnov coils, an interferometer, four chords of an x-ray pulse height analyzer, an NaI scintillation detector, a photodiode, two black and white CCD video cameras, several probes including a Mach probe, a triple probe, and swept Langmuir probes.

The magnetic diagnostics are necessary to reconstruct the equilibrium magnetic field and pressure profiles. Seven flux loops circling the vessel measure the magnetic flux along the z-axis. Eighteen pickup coils and eighteen Hall probes are positioned on the outside of the vacuum vessel to determine the magnetic field at their given locations. On the inside of the vessel two Mirnov coils, spaced 45 degrees apart measure the magnetic fluctuations of the plasma. Six more of these internal Mirnov coils will be installed in the near future.

A heterodyne interferometer views a chord across the vacuum vessel, which goes

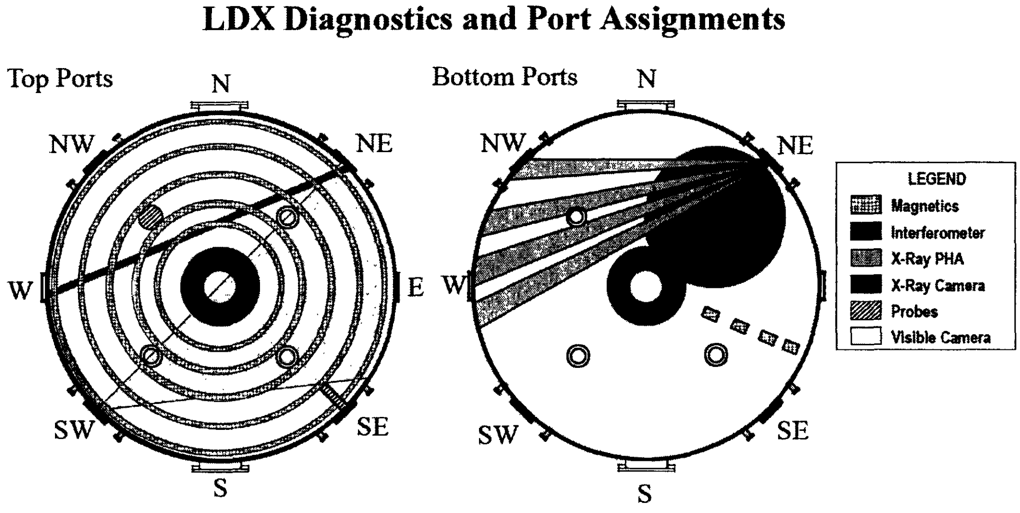

Figure 2-3: Initial diagnostic set of the Levitated Dipole Experiment.

near the coil, at a point where the density is assumed to be a maximum. The interferometer operates at a frequency of 60 GHz, and calculates a line averaged density. In the future, the interferometer will view several more chords in order to calculate a more accurate density profile.

Four chords of an x-ray pulse height analyzer view different regions of the plasma in approximately eight degree increments. An x-ray pulse height analyzer measures the energy spectrum of Bremsstrahlung radiation of the hot electrons by producing a charge proportional to the energy of the incident x-ray [12]. This information is then used to calculate the temperature of the hot electrons in the plasma. For one run , a sodium iodide scintillation detector was positioned to look directly at the F-Coil to help determine what conditions produce the most hot electrons by measuring the intensity of the x-ray emission. This detector now views a chord that passes through the pressure peak [12].

Two photodiodes are used to determine the intensity of the visible light emitted from the plasma. Also, two black and white CCD video cameras view the plasma. One camera is positioned at the top of the vessel, looking down at the plasma, while the other camera records a side view.

Several probes were used in the initial plasma runs such as swept Langmuir probes and a Mach probe. The swept Langmuir probes are at a fixed position during a shot while being swept in frequency to determine the edge density of the plasma. Between shots these probes can be moved into the best position for the next shot. A Mach probe measures the ion velocities in both directions in order to determine the direction and velocity of the plasma flow.

2.3 Typical Plasma Shot

LDX will normally create a plasma using deuterium as the fuel; however, other gasses such as hydrogen, helium and argon can also be used to create the plasma. The plasmas are created and heated using multiple frequency electron cyclotron resonance heating at 2.45 GHz and 6.4 GHz. Both of these sources can produce microwaves at power levels up to 3 kW.

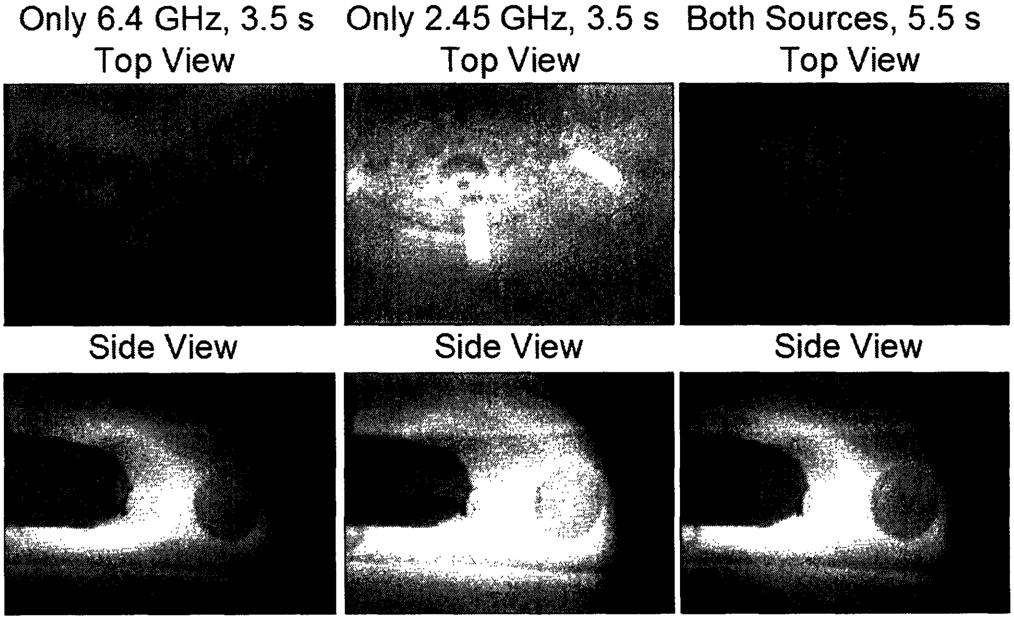

Figure 2-4: Top and side views of the plasma heated by 6.4 GHz only (left), 2.45 GHz only (middle), and both sources (right).

Having two sources available with variable powers creates many combinations of frequency and power that can be used to heat the plasma. Shown in figure 2-4, are

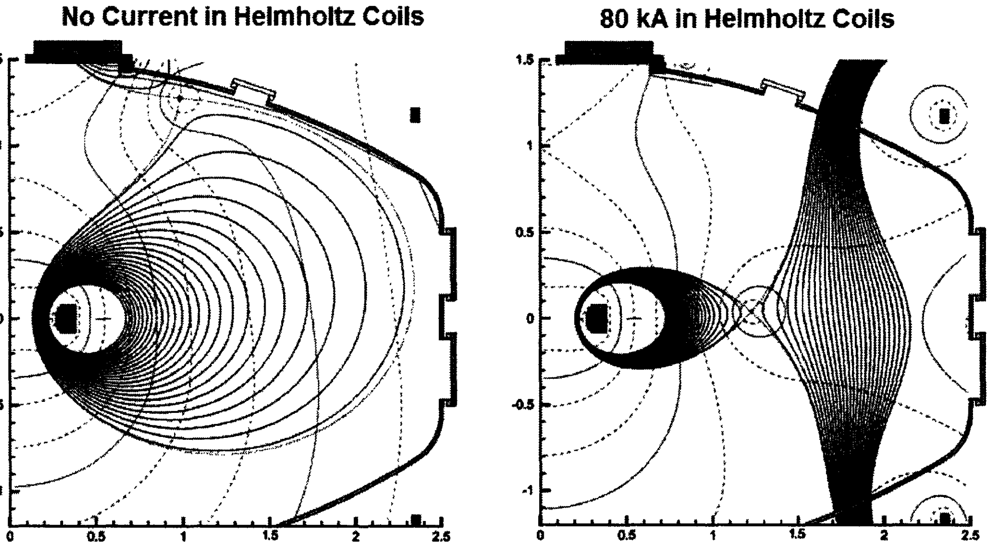

Figure 2-5: Magnetic geometry when the coil is levitated without any current in the Helmholtz coils (left) and with 80 kA in the Helmholtz coils (right).

pictures taken from the top and side CCD cameras of different shots when different combinations of frequencies were used to heat the plasma, all at 3 kW. These CCD cameras have automatic gain control, so the intensities cannot be compared; however, the spatial location of bright plasma rings can be qualitatively compared. In the future the addition of more sources at 10.5 GHz, 18 GHz, and 28 GHz will expand the number of combinations of frequencies and powers that can be used to heat the plasma.

Another variable of LDX is the Helmholtz Coils. When these coils are turned on, they produce a vertical field which can create a separatrix in the plasma if the currents are large enough. Depending on the currents in the upper and lower coils, many different magnetic field and pressure profiles can be obtained. In figure 2-5, the left image is the magnetic geometry for the case when the Helmholtz Coils are off, and the image on the right is when the Helmholtz Coils are carrying 80 kA of current. This equilibrium is for an idealized case using the Levitation Coil to levitate the F-Coil, which is at full current.

Another variable is the current in the F-Coil. Since the F-Coil is what creates the

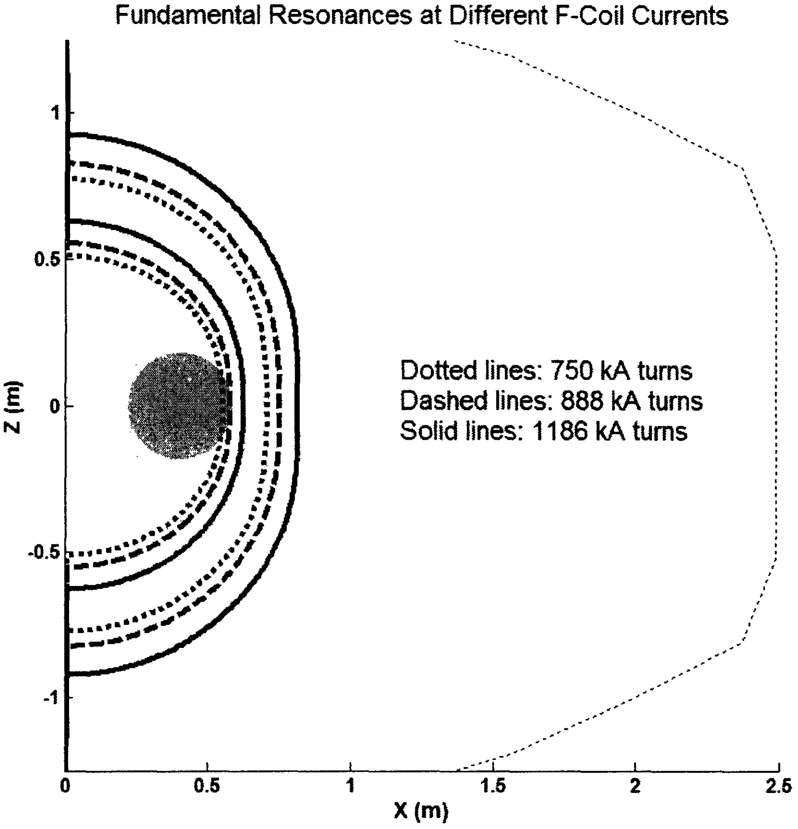

Figure 2-6: The fundamental resonances for F-Coil currents of 750 kA turns, 888 kA turns, and 1186 kA turns. The computer simulations for the rest of this thesis use an F-Coil current of 888 kA turns.

magnetic field, as the current in the F-Coil increases the magnitude of the magnetic field increases. Although changing the magnitude of the magnetic field does not change the shape of the field lines, it will change where the resonances and cutoffs appear. The fundamental and first harmonic resonances, as well as the right hand cutoff, are functions of the magnetic field magnitude. By increasing or decreasing the current in the F-Coil, these resonances and cutoffs will be shifted in toward the coil, or out away from the coil respectively. In our initial runs, the F-Coil has carried a current up to about 0.9 MA, approximately 888 kA turns in figure 2-6. In the near future the F-Coil will carry a current of 1.25 MA, which will shift the resonances and cutoffs out away from the F-Coil.

Based on the currents in all of the coils, and assuming absorption of 3kW at 2.45

Plasma Parameters			
	A	B	C
Helmholtz Coil Currents: Top, Bottom (kA)	0,0	1,12	50,50
Plasma Volume (m^3)	14	27	1.7
SOL Pressure (Pa)	0.25	0.25	0.25
Max Pressure (Pa)	1.35	1530	45
Plasma Current (kA)	3.2	16.4	0.39
Stored Energy (J)	315	1450	27
R(P_{max}) (m)	0.76	0.76	0.77
B(P_{max}) (Tesla)	0.088	0.088	0.088
$(P_(max))$ (Tesla)	0.08	0.55	0.015

Table 2.1: Plasma Parameters for different optimizations with the F-Coil levitated. Column A is for a plasma that is diverted but is not shaped by the Helmholtz coils. Column B is for a diverted plasma with the Helmholtz Coils at values which maximize beta. Column C is similar to B except the Helmholtz coils are at values to minimize beta.

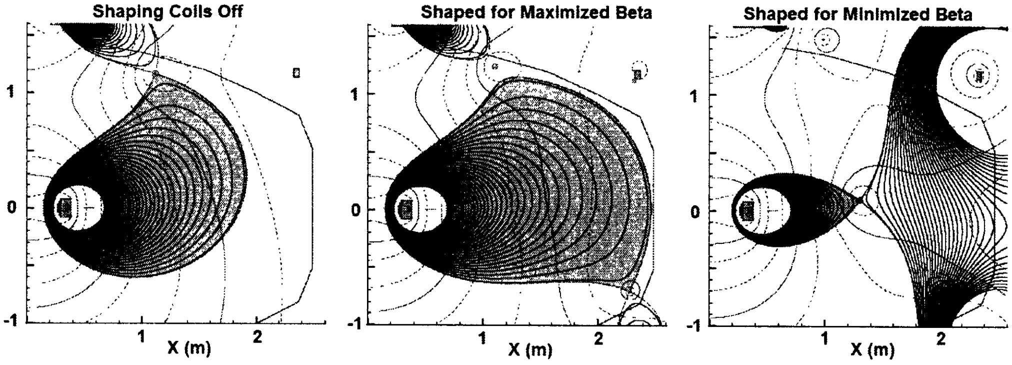
Shaping Coils Off

Shaped for Maximized Beta

Shaped for Minimized Beta

Figure 2-7: Different magnetic geometries for plasmas with the F-Coil levitated.

GHz and also at 6.4 GHz, computer simulations and calculations can be carried out to calculate expected parameters of the plasma. The pressure in the scrape off layer (SOL) of the plasma, the maximum value of the pressure, and the location where this maximum occurs, as well as the beta and the stored energy of the plasma can all be calculated. Table 2-1 lists the values for several chosen configurations assuming that the F-Coil is being levitated and at the full designed current of 1.5 MA, and figure 2-7 illustrates the magnetic geometry for these configurations.

Chapter 3

ECRH Heating Systems

The plasma in LDX is created and heated using multiple frequency electron cyclotron resonance heating. Although this system heats the electrons to temperatures of tens of keVs, the ions remain relatively cold at temperatures of a few eV. Currently the heating system is composed of a 2.45 GHz magnetron and a 6.4 GHz klystron, both capable of producing up to 3 kW of power. Waves from both sources are emitted into the vacuum vessel through antennas to cavity heat the plasma. In the near future a 10.5 GHz source will be directionally launched through the bottom of the vessel at powers up to 10 kW. In the further future 18 GHz and 28 GHz sources will be added to further heat the plasma and shape the pressure profile. This chapter will present information about the hardware as well as the triggering, data acquisition, and calibration of each system.

3.1 Hardware

3.1.1 2.45 GHz System

The 2.45 GHz system is powered by a Gerling magnetron, capable of producing up to 3 kW of power. Inside the magnetron, electrons are emitted from a central cathode. The anode surrounding the cathode attracts the electrons. Instead of traveling in straight lines, permanent magnets force the electrons to take a circular path. As they

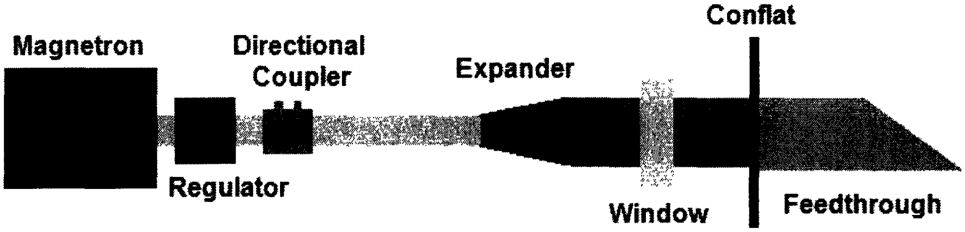

Figure 3-1: 2.45 GHz system.

pass by resonating cavities they generate a continuous pulsating magnetic field, or electromagnetic radiation.

The electromagnetic waves exit the magnetron in the TE_{10} mode and pass through a circulator. The purpose of the circulator is to protect the magnetron from reflected power. Along the waveguide run from the magnetron to the vessel there may be imperfections that cause part of the power to be reflected back towards the magnetron. Also, if the antenna is not cut at the correct angle, some power may be reflected back towards the magnetron. Circulators are designed to allow the waves to carry the power unobstructed in one direction while diverting any power flowing in the opposite direction. Our circulator allows the energy to flow from the magnetron towards the vacuum vessel while deflecting any power traveling in the opposite direction into a water-cooled dummy load.

Attached to the other side of the circulator is the directional coupler, a diagnostic used to determine the forward and reflected power traveling through a waveguide. The directional coupler has two probes that detect the electric field inside the waveguide. These probes are geometrically oriented to be able to distinguish between forward and reflected power. The signal from these probes is passed through a 60 dB attenuator, a DC block, another 10 dB attenuator, and into a Krytar 109B Zero Bias Schottky Detector Diode shown in figure 3-2. This diode converts the power into a voltage, with the conversion factor being 0.5 V/mW, which is analyzed and recorded.

Exiting the directional coupler, the waves travel through 6 meters of WR284 aluminum waveguide. A twelve-inch waveguide expander section expands from WR284

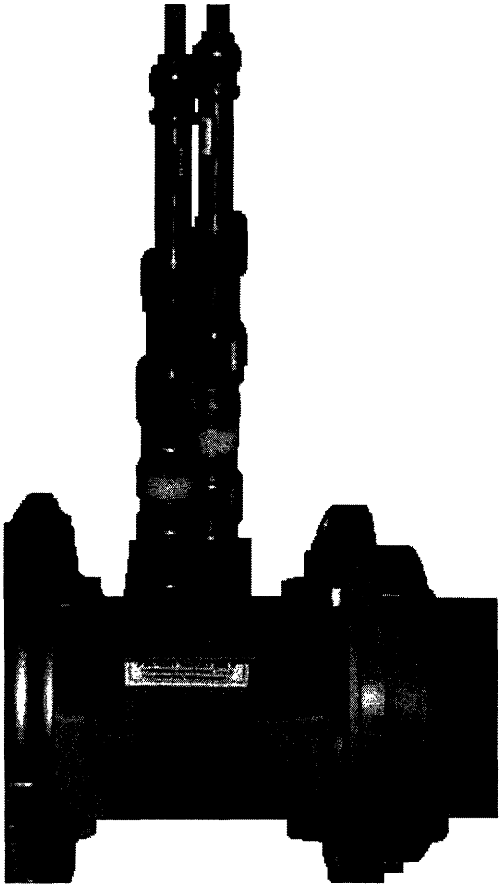

Figure 3-2: 2.45 GHz directional coupler with the DC block, attenuator, and detector diode attached.

to WR340 waveguide. Less than 2 meters of WR340 waveguide separates the expander and the vacuum window.

The waveguide window is where the waveguide switches from atmospheric pressure on the magnetron side to the vacuum pressure of the vessel on the antenna side. The waveguide holding the window is WR340 waveguide, which is why the expander section is needed. The window, shown in figure 3-3 is a ceramic, and is capable of being water-cooled, but since the magnetron only generates up to 3 kW of power water-cooling of the window is not needed.

The window attaches to the antenna section, which is a copper piece of WR340 waveguide silver-soldered into a stainless steel conflat. The vacuum side of the waveguide is cut at the Vlasov angle, 45 degrees, to minimize the reflected power and

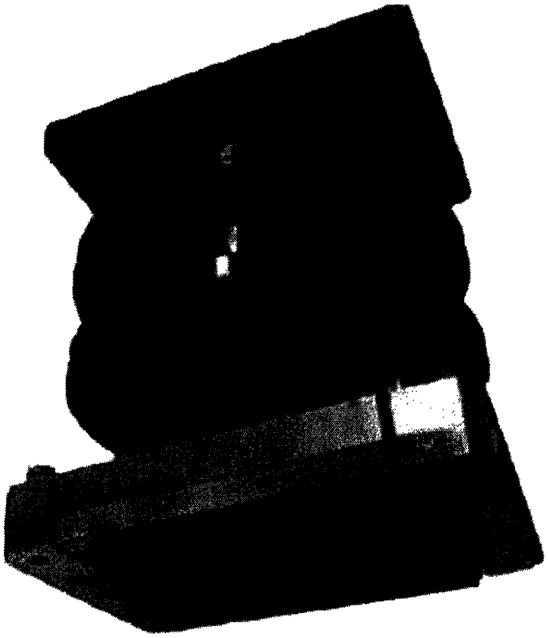

Figure 3-3: 2.45 GHz waveguide section with the window inside.

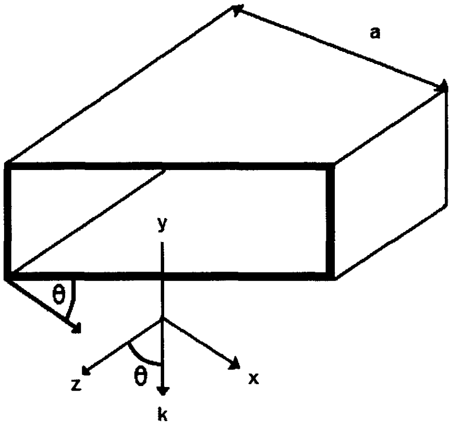

Figure 3-4: Diagram of a waveguide cut at the Vlasov angle.

to minimize the directionality of the launcher. For the TE_{10} mode: $k = k_x e_x + k_z e_z$ as shown in figure 3-4. The cutoff frequency is $\omega_{10} = \frac{c\pi}{a}$ where a is the large dimension of the waveguide. The Vlasov angle is determined by: $\cos(\theta) = \sqrt{1 - \left(\frac{\omega_{10}^2}{\omega^2}\right)}$, where ω is the input heating frequency.

The antenna, shown in figure 3-5 is positioned at the mid-plane of the vacuum

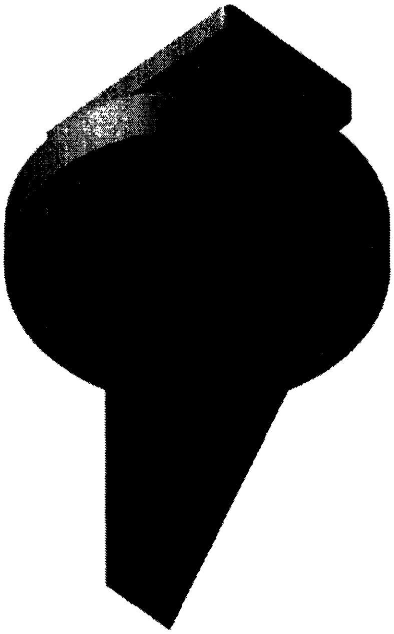

Figure 3-5: 2.45 GHz antenna and conflat.

vessel to launch in X-mode, where the electric field is perpendicular to the magnetic field. The waves are launched up in order to reach the top of the vessel and reflect to cavity heat the plasma and avoid toroidal directivity.

3.1.2 6.4 GHz System

The 6.4 GHz system is powered by a Varian klystron, capable of producing up to 3 kW of power. An electron gun produces an intense flow of electrons into the klystron,

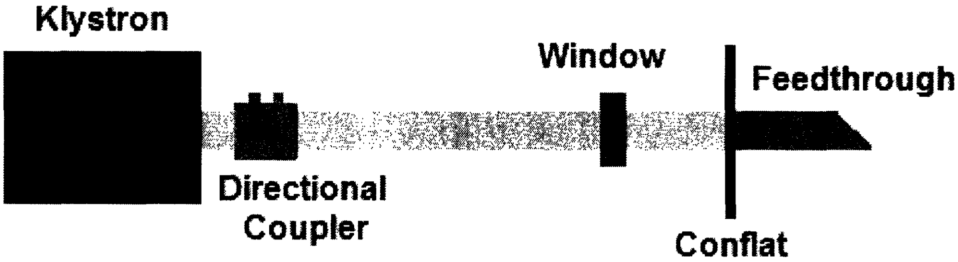
Klystron
Window
Feedthrough
Directional Coupler
Conflat

Figure 3-6: 6.4 GHz system.

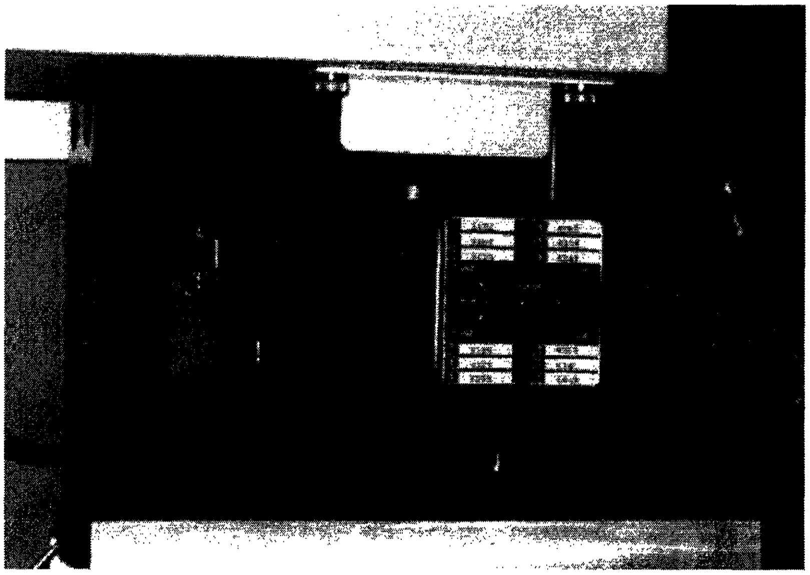

Figure 3-7: 6.4 GHz klystron.

pictured in figure 3-7. In the first cavity, a low-energy microwave signal intersects this continuous electron beam, breaking it up into a pulsed beam consisting of separate "bunches" of electrons. These electrons pass through a tuned drift tube into a second cavity where they are amplified and produce the microwaves. The microwaves enter the waveguide in the TE_{10} mode.

The directional coupler system for the 6.4 GHz system is in the cabinet and works basically the same way as the directional coupler system on the 2.45 GHz system, except that the directional coupler for the 6.4 GHz system has an attenuation of 50.1 dB. The 20 dB detector diodes came as part of the system, with the output being wired directly into the central logic of the system. One of the outputs from the cabinet is a 0 to 10 volt signal representing the forward power from 0 to 3 kW of power. There is no external output from the cabinet for the reflected power, so the signal coming from the reflected power detector diode is split and one of the signals is run to the digitizer to be analyzed and recorded, the same way the signals are recorded for the 2.45 GHz system.

When the WR137 aluminum waveguide exits the cabinet, it travels about 20 meters to the quartz vacuum window. Similar to the function of the 2.45 GHz window,

Figure 3-8: 6.4 GHz window.

the 6.4 GHz window, shown in figure 3-8, separates the vacuum pressure in the vessel from the atmospheric pressure in the waveguide.

The antenna for the 6.4 GHz source is again similar to that of the 2.45 GHz system. It consists of a copper piece of WR137 that runs through a stainless steel conflat and is silver-soldered to seal it. The vacuum side of the antenna is cut at the Vlasov angle which, for this size of waveguide, is approximately 42 degrees as seen in figure 3-9. This antenna is located at the same side port as the 2.45 GHz antenna, at the mid-plane of the vacuum vessel. It also launches the waves in X-mode in order to avoid directionality and reach the top of the vessel and scatter to cavity heat the plasma.

The 10.5 GHz system that should be operational by this summer consists of a klystron that is capable of producing up to 10 kW of power. Again, there are directional couplers with detection diodes on the waveguide where it leaves the klystron. There is about a 15 meter run of WR90 waveguide to the bottom of the vessel where it will be launched with the long axis of the waveguide running parallel to the magnetic field.

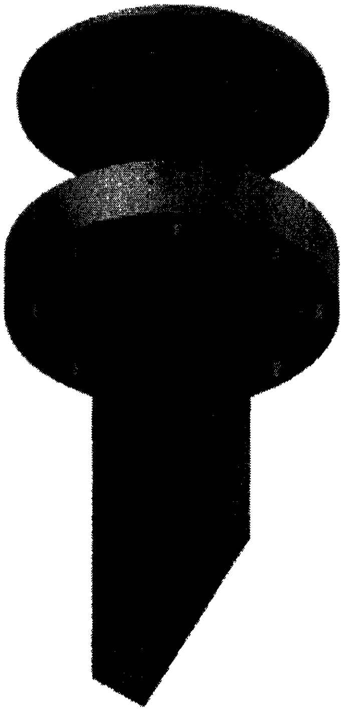

Figure 3-9: 6.4 GHz antenna and conflat.

3.2 Triggering

To begin a shot, a signal is sent out from the control computer to the timing system, a Jorway 221 (J221) timer. The outputs of the J221 are then passed through a Jorway 222 (J222) line driver, which sends the signal to several diagnostics and other systems, such as the ECRH system. The signal out of the J222 is a Transistor Transistor Logic (TTL) signal, which is a 5 volt maximum digital signal. For both the 2.45 GHz and the 6.4 GHz systems, their TTL signals travel a few feet to a box where there are two passive (no extra power supply required) Fiber Optic Transmitters from VI controls, one for each source. These passive transmitters convert the TTL signal into a fiber optic signal. The fiber optic cables are run across the cell to the ECRH sources; however, the triggering of the two sources occurs differently.

The 2.45 GHz magnetron can be operated in two modes: manual or remote. In the remote mode a TTL signal is the required input to turn the system on. The

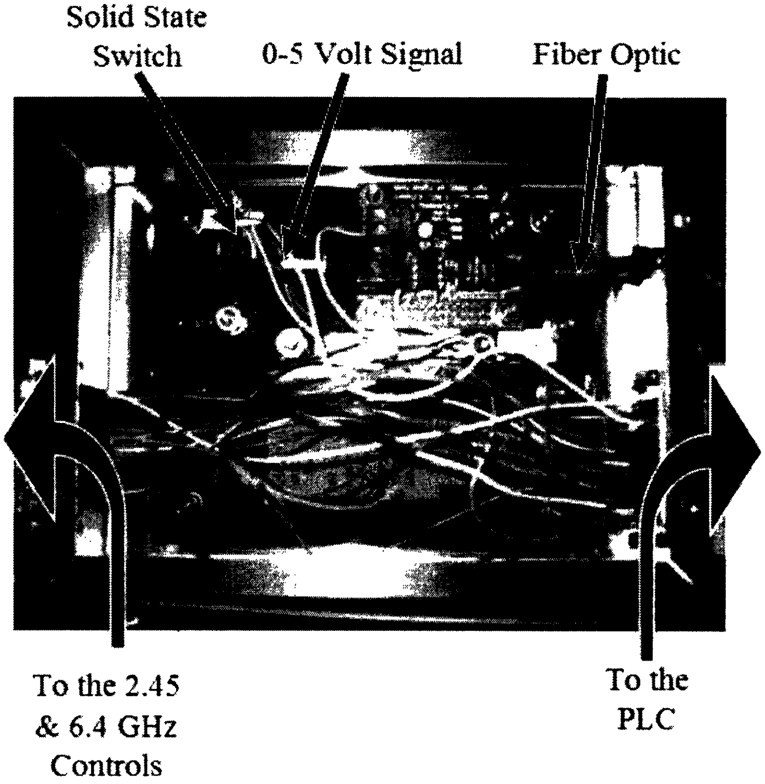

Figure 3-10: Triggering system including the fiber optic converter and switch.

power level is set by a knob in the front of the magnetron, so when it is turned on and receives the TTL signal, the microwaves are emitted into the waveguide with the specified power. On this end of the fiber optic cable, an Active Fiber Optic Receiver is used to convert the fiber optic signal back into a TTL signal. The "active" part of the receiver simply means that it requires 5 volts to operate.

However, in the remote mode, when the system is powered on, the magnetron constantly emits 30 watts of power. This is not enough to create a plasma when we want the system to be off, but 30 watts of power going into the vessel at all times is not acceptable. To keep the output power at 0 watts instead of 30 watts when the magnetron is supposed to be off, a contact on a Programmable Logic Controller (PLC) is used, which is controlled by the main computer. In order for the magnetron to emit even the 30 watts, this contact must be closed. This is activated by an initial pulse from the J222 which occurs right before the pulse that sends the signal to turn the magnetron on to the selected power, and the node is deactivated right after the pulse of power in order to stop completely the power from being emitted.

The triggering for the 6.4 GHz is somewhat simpler than that of the 2.45 GHz system. Fortunately, when the 6.4 GHz system is in remote operation mode it really can turn off and does not emit any power. There is a "RF Inhibit" function that will cut off the low-energy microwave signal before it is amplified to keep the klystron from emitting any power. To trigger the system, the signal from the fiber optic cable enters an Active Fiber Optic Receiver that changes the fiber optic signal into a TTL signal. This signal is run into a solid state switch shown in figure 3-10, where the 5 volts cause the switch to close. By connecting the two ends of the switch to the inputs for the "RF Inhibit" function, the power from the klystron can be switched on and off by the signal coming through the fiber optic cable.

3.3 Data Acquisition

Each detector diode produces a signal voltage which is proportional to the amount of power it is detecting. The two detector diodes for the 2.45 GHz system are external, and a BNC cable attaches to the back of the diode pictured in figure 3-11. The forward power from the 6.4 GHz is transferred from the central logic of the cabinet through two pins on a 50 pin connector, whereas the reflected power's diode runs directly into an SMA cable. The two BNC cables from the 2.45 GHz system, the SMA cable from the 6.4 GHz system, and the two wires from the 50 pin output from the 6.4 GHz cabinet are all run to the top of the 6.4 GHz cabinet where they are soldered onto 8 wires in a shielded CAT5 cable.

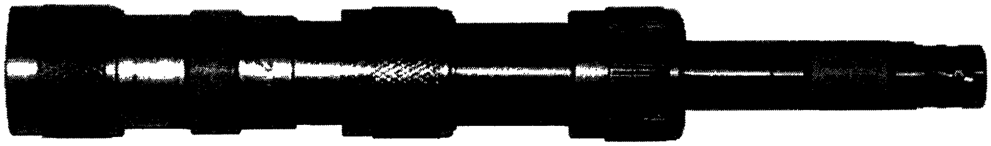

Figure 3-11: DC block, 10 dB attenuator, and Zero Bias Schottky Detector Diode.

The signals are run via the CAT5 cable in twisted pairs over to the other side of the cell where they are digitized. Since the digitizer can handle up to 10 volts, and the signal coming from the 6.4 GHz cabinet is supposed to range from 0 to 10 volts, the forward and reflected power signals are divided by two before they reach the digitizer cabinet, making the range approximately 0 to 5 volts.

All four signals are fed into the back of the digitizer cabinet via the CAT5 cable. They run through a ribbon cable to an amplification board. Since the 6.4 GHz signal is already 0 to 5 volts, which is right in the middle of the range of the digitizer, the amplification board really only serves as an isolator for the 6.4 GHz signal. The amplification factor is 1 to 1, but the amplification board takes the incoming signal and keeps the ground for the ECRH sources and the ground for the digitizer cabinet separate.

The 2.45 GHz signals are much weaker than the signal coming from the 6.4 GHz cabinet, due to the use of a 10 dB attenuation stage to protect the diodes, so the amplification board for the 2.45 GHz signal serves two purposes. It keeps the grounds separate, as it does for the 6.4 GHz system, and it also amplifies the signal. The signal out of the detector diodes for the 2.45 GHz system ranges from 0 to 100 mV, so the signal is multiplied by approximately 50 on the amplification board in order to make the signal range from 0 to 5 volts. From the amplification board the signal goes to the D-Tac 200 digitizer boards, which digitize at a rate of 125 kHz (from Alcator C-Mod).

3.4 Calibration

A relatively "first order" calibration has been carried out of both systems. The voltage recorded by the digitizer has been approximately calibrated to the forward and reflected power in the waveguides, and the dial setting on the sources has been calibrated with respect to the forward power in the waveguides. In the future if more exact values of the power launched into the vessel are needed, a new calibration will need to be performed. There are several aspects of the systems that can be calibrated.

If the attenuations of the directional coupler and detector diodes are known, one can calculate the conversion factor between the signal voltage and the power flowing in the waveguide. Another way to calibrate the system is to take the voltage recorded by the digitizer and compare it to the power dial setting of the source. Both sources also have an LCD that reads out the forward power from an internal calibration of the source. This can also be calibrated against the voltage recorded by the digitizer. Probably the most useful calibration when trying to set the source to produce the correct power is a calibration of the dial setting and the LCD readout of the forward power. If the attenuation of the directional coupler as well as the attenuation of the detector diodes is known, a conversion factor between the signal voltage and the power transmitted through the waveguide can be calculated. The signal's path through voltage dividers and amplifiers is known, so an overall conversion factor between the voltage recorded by the digitizer and the power flowing through the waveguide can be detected. For example, all of this information is known for the 2.45 GHz system, so this calculation is possible. The 2.45 GHz signal passes through directional coupler which has an attenuation of 60 dB, then the signal passes through a DC block of 0.2 dB, then through another 10 dB attenuator, and finally to the diode which has a conversion factor of 0.5 V/mW. Finally, the amplification board multiplies the signal 47 times before it reached the digitizer. With a 1.0 dB tolerance for the attenuators, the upper (equation 3-1) and lower (equation 3-2) bounds on a calibration can be calculated, which are not very accurate:

$$10^{-\frac{61+0.2+1.1}{10}} * \frac{0.5Volts}{10^{-3}Watt} * 47.5Amplification = 1.416 * 10^{-3}V/W \Rightarrow 0.706kW/V \tag{3.1}$$

$$10^{-\frac{59+0.2+0.9}{10}} * \frac{0.5Volts}{10^{-3}Watt} * 47.5Amplification = 3.556 * 10^{-3}V/W \Rightarrow 0.281kW/V \tag{3.2}$$

Although this calculation determines what the conversion factor between voltage and power should be ideally, there are potential errors that would affect this conversion factor. The diodes are supposed to have a linear response to power, but there is potential that there are some non-linear portions in the range of the detector. Another possible source of error is the geometric orientation of the probes in the directional coupler. The power detected is very sensitive to the geometric position of the probes, and having a probe slightly misaligned will hurt the accuracy of the data and the directional coupler will have to be re-oriented by the manufacturer.

Both the 2.45 GHz and the 6.4 GHz sources detect the forward power emitted and display the power on an LCD. This allows for a comparison of the voltage recorded by the digitizer to the forward power detected by the sources and displayed on the LCDs.

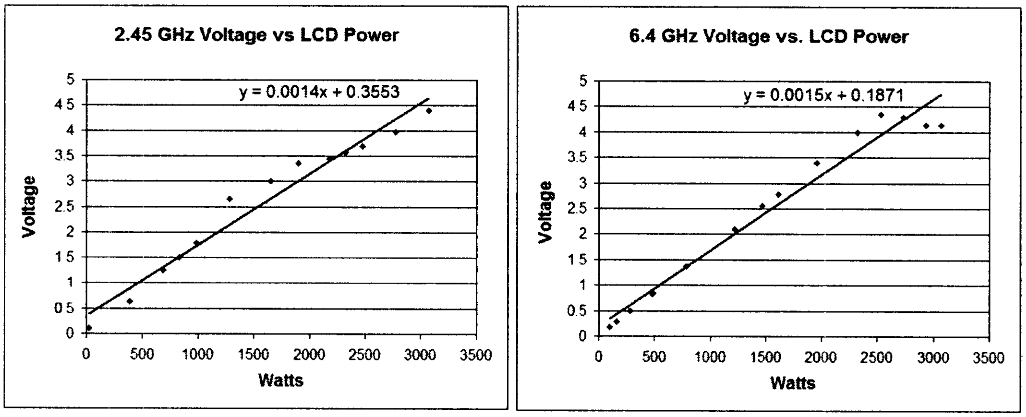

Figure 3-12: Calibration plots of signal voltage versus power.

The slope of the best fit line is the conversion factor of volts per watt. The voltages follow the best fit line decently well, except for the high power of the 6.4 GHz system as seen in figure 3-12. At powers above 2500 watts the voltage actually decreases. This non-linearity of the 6.4 GHz system's power detection system does not allow a precise determination of the power based on the data. For the current plasma runs, this is not a problem since we are not performing detailed power scans. We do know that when the dial is set on the source, the same amount of power is produced every time that the dial is at a specified setting.

Although the data cannot determine the power exactly, there is a relatively linear

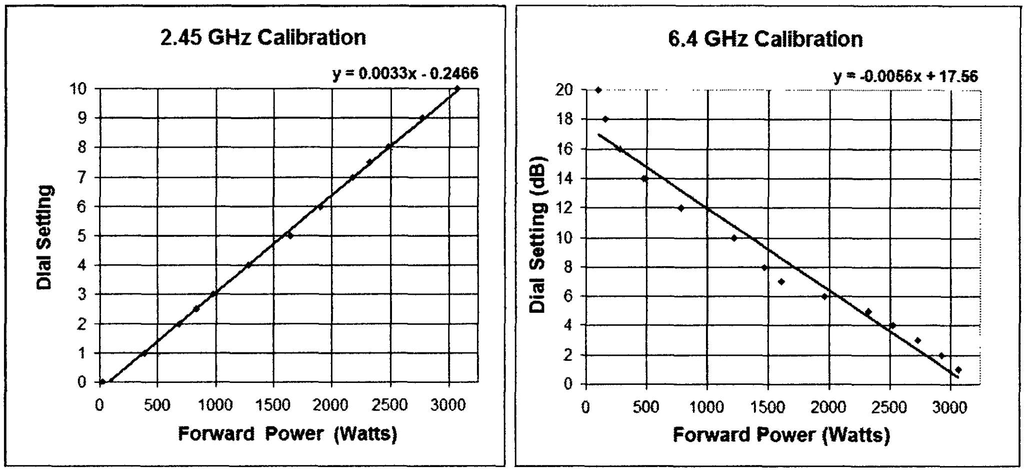

Figure 3-13: Calibration plots of source dial setting versus power.

relationship between the dial setting and the power emitted. The 2.45 GHz system has a fractional dial that is linearly correlated with the power emitted. The 6.4 GHz system has a dial that controls the attenuation so when the dial is at the highest number, 20 dB, it emits the minimum power.

These are the most useful calibrations when making a plasma shot. When the power desired is determined, the appropriate dial settings can be looked up on these plots shown in figure 3-13.

3.5 Typical Plasma Shot

During a run day for LDX the floating coil (F-coil), that generates the dipole field, is charged once or twice. Each time the coil remains superconducting for about 150 minutes while plasma shots are taken. The coil can be charged to different currents, which produce magnetic fields of different magnitudes. Since the F-coil is superconducting, the current and magnetic field remain relatively constant until the coil quenches.

Electron cyclotron resonance heating is based on the electron cyclotron frequency, $\omega_{ce} = \frac{lqB}{\gamma m_e}$, where l is the harmonic, q is the electron charge, B is the magnetic field, m_e is the electron mass, and $\gamma = \sqrt{\frac{1}{1+\frac{v^2}{c^2}}}$ is for relativistic corrections. The heating

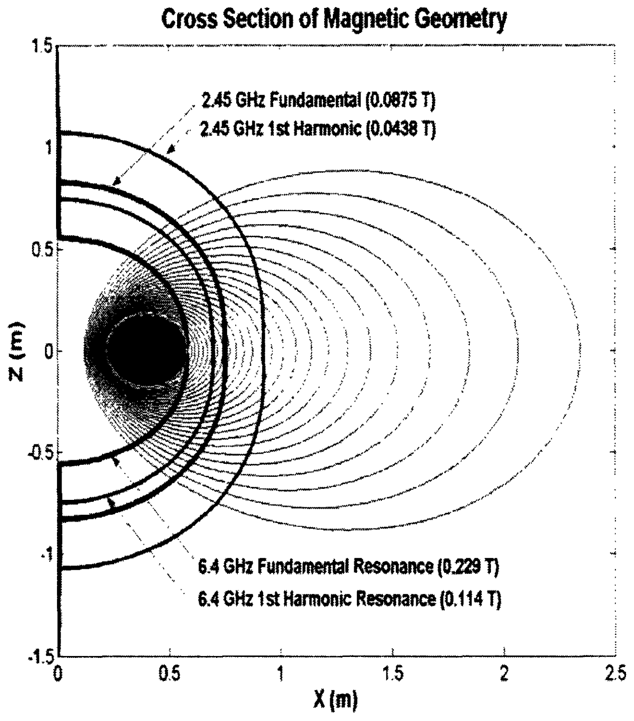

Figure 3-14: Fundamental and first harmonic resonances for both sources.

wave will resonate with the electrons when the electron cyclotron frequency matches the heating wave's frequency. The resonances lie along lines of constant magnetic field amplitude as shown in figure 3-14.

The magnitude of the magnetic field, and therefore the location of the resonances, can be calculated as follows: $B(r) = \frac{2\pi f \gamma m_e}{lq}$. For the 2.45 GHz heating, the fundamental resonance will be where the magnitude of the magnetic field is 0.0875 Tesla, and the first harmonic will be at 0.0438 Tesla, assuming $\gamma = 1$. Based on the measured temperatures of the plasma so far, this assumption is valid. The 6.4 GHz source has resonances at higher magnetic field strengths: the fundamental is at 0.229 Tesla and the first harmonic is at 0.114 Tesla. The future sources of 10.5 GHz, 18 GHz, and 28 GHz will have their resonances at even higher magnetic field magnitudes. Using an equilibrium reconstruction code developed by Darren Garnier, DIPEQ [15], the value of the magnetic field is calculated at all points in space. The code calculates a free boundary solution to the Grad-Shafranov equation by using Green's functions to update the boundary conditions and re-solving the Grad-Shafranov equation iteratively. Using this information a plot of the magnetic field lines and lines of constant magnetic field magnitude can be generated to show where the resonances are in physical space.

One of the side ports of LDX has a visible camera that views the coil and plasma. Combining a frame from the camera, where a bright ring is seen, with a plot of where the resonances are shows that the bright ring of hot electrons is tangent to the resonant surface. The magnetic field line that is tangent to the resonant surface should be heated the most, since the electrons are in the resonant zone for a longer time than the electrons that are on a magnetic field line that crossed the resonant surface at an arbitrary angle. By matching the position and size of the F-coil, the two images can be assured to be spatially correct, as shown in figure 3-15.

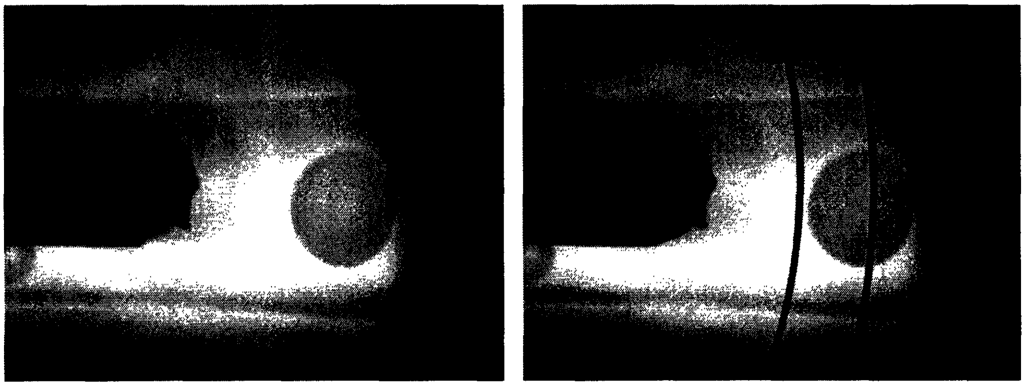

Figure 3-15: Picture of plasma formed by the 2.45 GHz source (left). Same picture with the fundamental and first harmonic resonances superimposed (right). (shot: 50317015)

Since LDX currently has two sources with variable power up to 3 kW each, there are several combinations of power levels and times that have been examined. Some of the plasma shots we have examined are heated by the 2.45 GHz alone, 6.4 GHz alone, both together, and one source on and the other source turning on and off. Several plasma shots have been taken with the sources at half power, although this has not been studied in as much detail as the shots with the sources at full power. Figure 3-16 is an example of the data from a modulation shot.

One interesting difference between the heating of the 2.45 GHz source and the 6.4

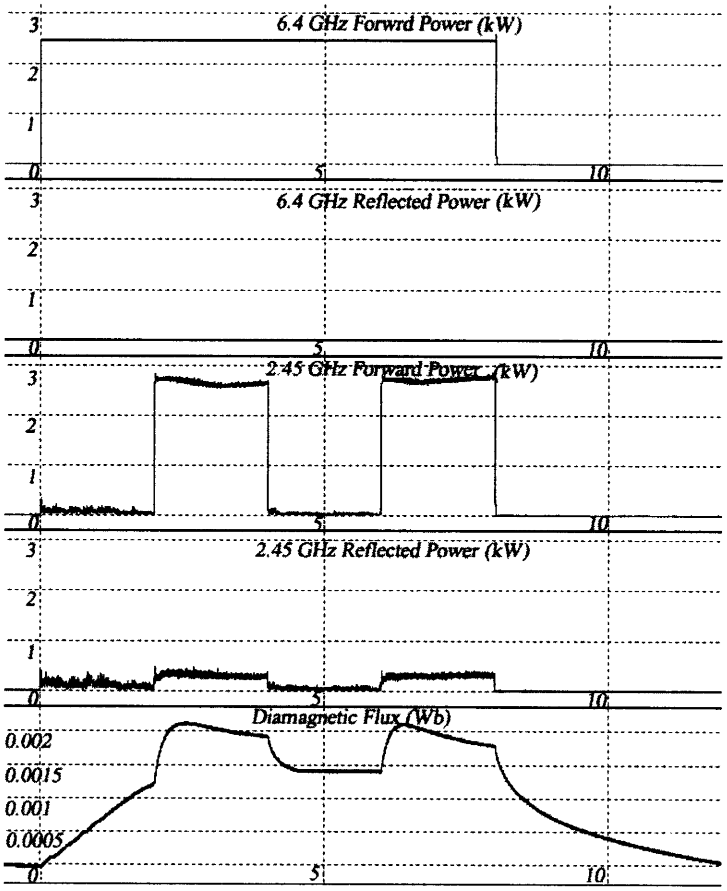

Figure 3-16: Data from a modulation shot where the 6.4 GHz source was on from 0 to 8 seconds and the 2.45 GHz source was turned on and off.

GHz source is the rate at which they change the diamagnetic flux. The 2.45 GHz source causes a much faster increase in the diamagnetic flux than the 6.4 GHz source. While the reason for this difference is unclear, it has been hypothesized that the 2.45 GHz source increases the diamagnetism faster than the 6.4 GHz source because for 6.4 GHz the mod-B surface is tangent to a field line that is very close to the coil and heating is inhibited by this field line hitting the coil. Therefore the 6.4 GHz source can only heat more weakly away from the point of tangency. Figure 3-17 compares shot 50318001 which utilized the 2.45 GHz source only with shot 50317012 which used the 6.4 GHz only, both at the maximum dial setting for the power.

The rise and decay time constants for the diamagnetic flux have been calculated using a nonlinear fit to the data assuming exponential behavior and the time constants

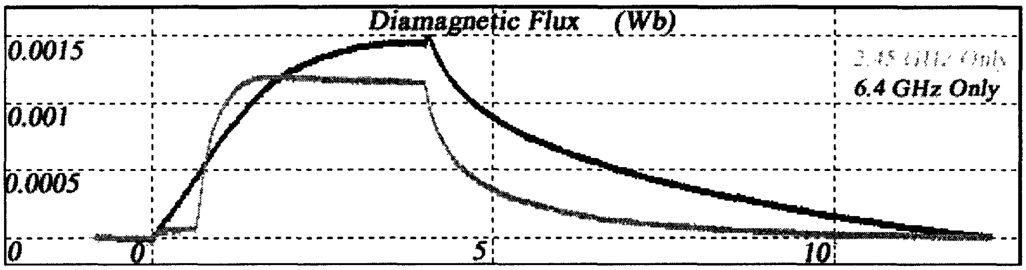

Figure 3-17: Comparison of diamagnetism from the 2.45 GHz (shot: 50318001 in gray) and 6.4 GHz (shot: 50317012 in black) sources.

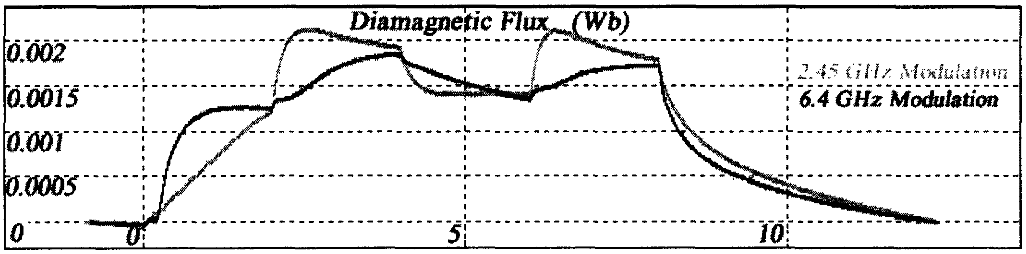

Figure 3-18: Comparison of diamagnetism from the 2.45 GHz and 6.4 GHz sources during a modulation shot. In shot 50318009 (black) the 6.4 GHz system is modulated, and in shot 50318007 (gray) the 2.45 GHz system is modulated

for both the rise and the decay satisfy $\tau_{2.45} < \tau_{2.45+6.4} < \tau_{6.4}$ [7]. The rise times during a modulated shot can be compared by overlaying the diamagnetic flux of two shots, as shown in figure 3-18. In one shot, 50318009, the 2.45 GHz source was on at 3 kW for 8 seconds and the 6.4 GHz source was turned on and off at 3 kW for 2 seconds at a time, from 2 to 4 seconds and from 6 to 8 seconds. The second shot, 50318007, uses the same timing, but with the 6.4 GHz source on at 3 kW the whole time and modulating the 2.45 GHz source.

Here again we see that the rise time of the diamagnetic flux for the 2.45 GHz source is much faster than the rise time of the 6.4 GHz source. In the time intervals from 2 to 4 seconds and from 6 to 8 seconds the grey curve, when the 2.45 GHz was turned on, increases much faster than the black curve, when the 6.4 GHz was turned on.

Another interesting aspect of many of our plasma shots is the formation of three distinct regimes: a low density regime, a high density regime, and an afterglow. In the following shot, 50317014, these three regimes are easily observable in figure 3-19. From zero seconds to about 0.25 seconds the plasma is in the low density regime. At about 0.25 seconds there is a quick transition to the high density regime. When the ECRH power is turned off at four seconds the afterglow lingers for a few seconds.

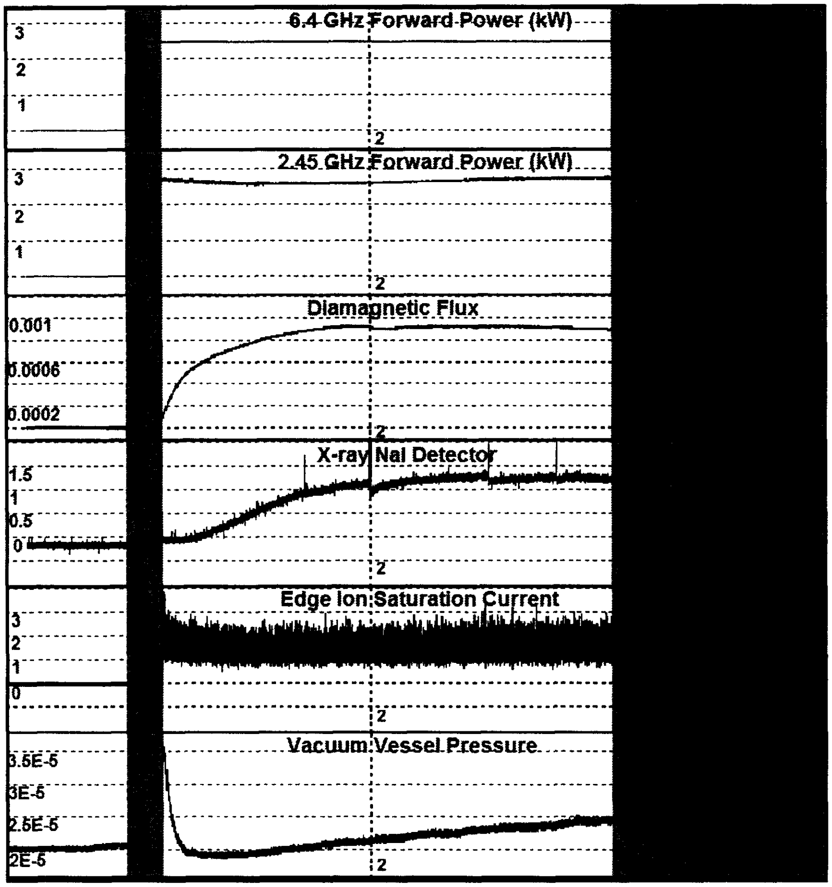

Figure 3-19: Data from a shot showing the low density (0-0.25 sec), high density (0.25 sec - 4 sec), and afterglow (after 4 sec) regimes.

The low density regime can vary in length; however, it typically lasts for less than a second. During the low density regime the NaI scintillation detector, which views the F-Coil, detects a considerable amount of x-rays. This signal means that there are numerous hot electrons striking the coil and producing these x-rays [18]. Also the edge probe records negative bursts in the ion saturation current. These negative bursts suggest that Hot Electron Interchange (HEI) instability is excited [17].

This low density regime is usually seen when the 2.45 GHz source is heating the plasma. Electrons are first heated on the fundamental resonance, and once the electrons are warm, the first harmonic heating accelerates them to very high energies. For the currents in the F-Coil that we have been using in our initial runs the fundamental resonance for the 6.4 GHz source will intersect the coil. It has been suggested that when heating with the 6.4 GHz source, the electron heating at the fundamental frequency takes place away from the midplane and therefore creates a broad pressure profile which remains stable to HEI [18].

In the high density regime the plasma is absorbing the ECRH power and heating. During this period the diamagnetism gradually increases, as does the x-ray signal from the NaI detector. At four seconds, the ECRH sources are turned off and the plasma moves into the afterglow regime. The background plasma is lost right away, but the hot electrons remain for a few seconds, sometime up to ten or fifteen seconds. During this time the diamagnetism slowly decreases as the hot electrons are gradually lost.

Chapter 4

Plasma Resonances and Cutoffs

Electron cyclotron resonance heating relies on the fact that there are resonances at the harmonics of the electron cyclotron frequency. As discussed in Chapter Three, the cyclotron frequency is a function of the magnetic field and since the magnetic field is a function of position, the cyclotron frequency is also a function of position. Although the majority of the power absorption takes place at the fundamental and first harmonic of the electron cyclotron frequency, there are other resonances and cutoffs that are important to understanding the wave propagation in the plasma. We will discuss the upper and lower hybrid resonances, the right hand cutoff, and the high density cutoff

4.1 Cold Plasma Dispersion Relation

The cold plasma dispersion relation accurately identifies the basic resonances and cutoffs in plasma. However, in the vicinity of a resonance this dispersion relation breaks down and hot plasma kinetics is needed to analyze the resonance. In "Stix notation" the cold plasma dispersion relation can be expressed as follows [13]:

$$\tan^2\theta = -\frac{P(n^2-R)(n^2-L)}{(n^2-P)(Sn^2-RL)} \tag{4.1}$$

where the P, R, L, and S are:

$$P = 1 - \sum_j \frac{\omega_{pj}^2}{\omega^2} \tag{4.2}$$

$$R = 1 - \sum_j \frac{\omega_{pj}^2}{\omega(\omega + \omega_{cj})} \tag{4.3}$$

$$L = 1 - \sum_j \frac{\omega_{pj}^2}{\omega(\omega - \omega_{cj})} \tag{4.4}$$

$$S = \frac{1}{2}(R + L) \tag{4.5}$$

and the plasma frequency and cyclotron frequency are:

$$\omega_{pj} = \left(\frac{n_j q_j^2}{\varepsilon_o m_j}\right)^{\frac{1}{2}} \tag{4.6}$$

$$\omega_{cj} = \left(\frac{q_j B}{m_j}\right) \tag{4.7}$$

and n is the index of refraction, k is the wave vector, and c is the speed of light:

$$n = \left(\frac{kc}{\omega}\right) \tag{4.8}$$

4.1.1 Resonances

A resonance is defined as when n^2 goes to infinity. We will look at wave propagation perpendicular to the magnetic field, where $\theta = \frac{\pi}{2}$. This causes $\tan^2\theta$ to go to infinity meaning that the denominator equals zero: $(n^2 - P)(Sn^2 - RL) = 0$.

The first possibility is if $(n^2 - P) = 0 \Rightarrow n^2 = P = 1 - \sum_j \frac{\omega_{pj}^2}{\omega^2}$. However, for the low densities measured in LDX, P does not vanish and this term does not lead to a resonance. The second possibility is if $(Sn^2 - RL) = 0 \Rightarrow n^2 = \frac{RL}{S}$ which will go to infinity when S goes to zero:

$$S = \frac{1}{2}(R+L) = \frac{1}{2}\left(1 - \sum_j \frac{\omega_{pj}^2}{\omega(\omega+\omega_{cj})} + 1 - \sum_j \frac{\omega_{pj}^2}{\omega(\omega-\omega_{cj})}\right) = 0 \tag{4.9}$$

By neglecting terms of order $\frac{m_e}{m_i}$, this simplifies to the upper and lower hybrid resonances:

$$\omega_{UH}^2 = \omega_{ce}^2 + \omega_{pe}^2 \tag{4.10}$$

$$\omega_{LH}^2 = \frac{\omega_{ce}^2 \omega_{pi}^2}{\omega_{ce}^2 + \omega_{pe}^2} \tag{4.11}$$

Lower hybrid resonances in the range of the frequencies with which we are heating are not located in the plasmas of LDX. The upper hybrid resonance is slightly higher than the electron cyclotron frequency and usually appears between the fundamental and first harmonics in our plasmas. Assuming a density profile of $n = C\psi^2$ the resonances would be as shown in figure 4-1.

4.1.2 Cutoffs

A cutoff is defined as when n^2 goes to zero, with $n = \frac{kc}{w}$, and for a wave to be propagating its k-vector must be real. We will look at wave propagation parallel to the magnetic field, where $\theta = 0$. The causes $\tan^2\theta$ to go to zero meaning that the numerator equals zero: $P(n^2 - R)(n^2 - L) = 0$.

The first possibility is if $P = 0$, which will produce the density limit for perpendicular propagation: $n_\perp^2 = P = 0 = 1 - \frac{\omega_{pe}^2}{\omega^2} - \frac{\omega_{pi}^2}{\omega^2} = 1 - \frac{\omega_p^2}{\omega^2} = 0 \Rightarrow \omega = \omega_{pe}$. This describes a cutoff where $\omega = \omega_p$ shown in figure 4-2. Since ω is the input frequency and ω_p is only a function of density, this cutoff is where the wave will not propagate because the density is too high.

The next possibility is if $(n^2 - R) = 0$, and since we are looking for a cutoff where n goes to zero, $n^2 = 0 = 1 - \sum_j \frac{\omega_{pj}^2}{\omega(\omega+\omega_{cj})}$. By neglecting terms of order $\frac{m_e}{m_i}$, this simplifies to the right hand cutoff:

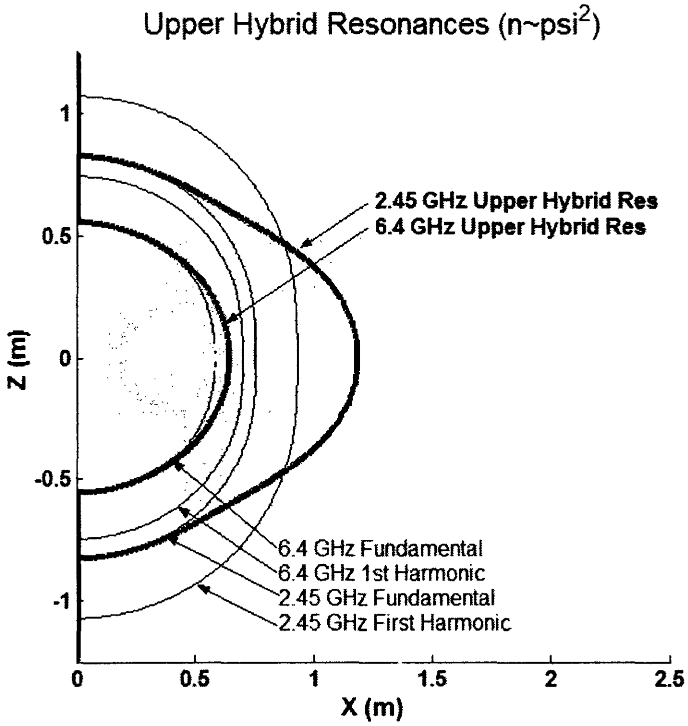

Figure 4-1: Upper hybrid resonances for both frequencies.

$$\omega_R = \frac{1}{2}\left(|\omega_{ce}| + \left(|\omega_{ce}^2| + 4\omega_{pe}^2\right)^{\frac{1}{2}}\right) \tag{4.12}$$

The other possibility of $(n^2 - L) = 0$ will produce the left hand cutoff, which will look similar to the right hand cutoff shown in figure 4-3:

$$\omega_L = \frac{1}{2}\left(-|\omega_{ce}| + \left(|\omega_{ce}^2| + 4\omega_{pe}^2\right)^{\frac{1}{2}}\right) \tag{4.13}$$

However, since electrons are right hand circularly polarized, this cutoff is not important in this study of ECRH.

4.1.3 Effect of Density on Resonances and Cutoffs

The density of the plasma has important impacts on several cutoffs and resonances. The fundamental and first harmonic cyclotron resonances are not a function of density; they both just depend on the magnetic field. However, the upper and lower

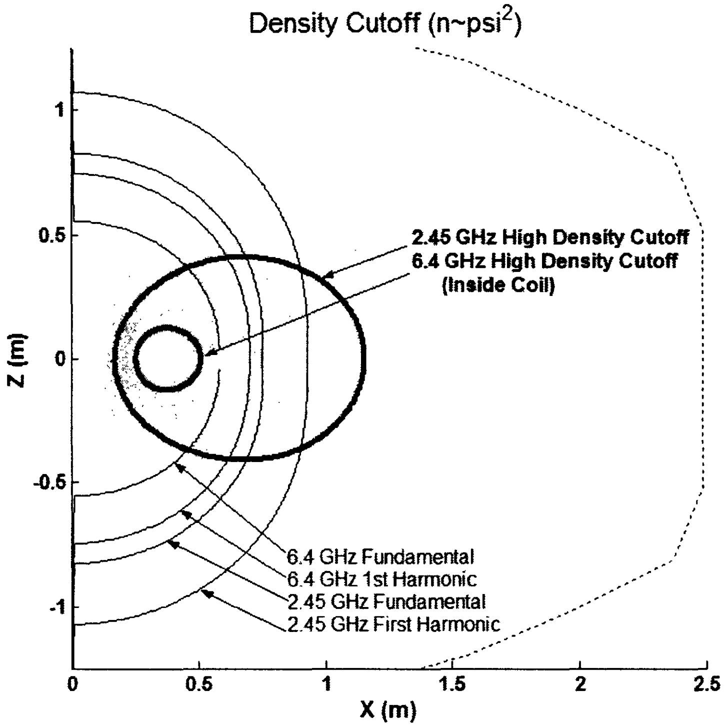

Figure 4-2: Density cutoffs.

hybrid resonances as well as the right hand cutoff and the high density cutoff are all functions of the local density. Therefore, it is important to know the spatial density profile in order to determine the location of the cutoffs and hence the accessibility of the resonances.

Our diagnostic set includes several flux loops, Mirnov coils, an interferometer, four chords of an x-ray pulse height analyzer, an NaI scintillation detector, a photodiode, and several probes including a mach probe, a triple probe, and Langmuir probes.

At present we cannot determine the density profile due to the limited diagnostic set. The probes detect the density at their location on the edge of the plasma, but they cannot be moved far into the plasma because of the temperature. The interferometer measures a line-averaged density across the plasma. The interferometer trajectory goes through the region of peak pressure and we assume it is the region of peak density as well.

Since we cannot calculate the exact density profile, we make assumptions in order

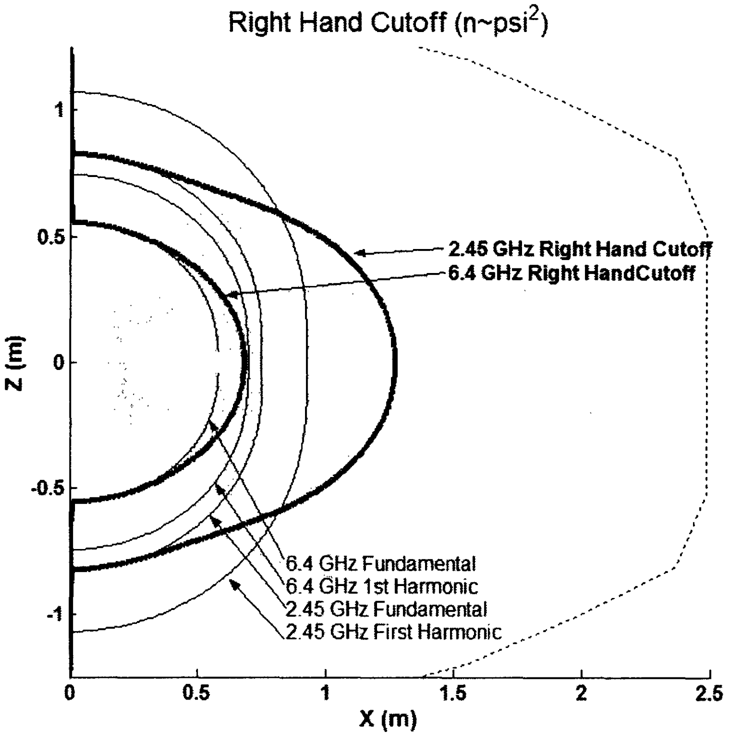

Figure 4-3: Right Hand Cutoffs for both frequencies.

to approximate possible density profiles. First we will assume density is constant on a field line, although this is not strictly true when there are end losses to the supports. Another assumption is that the density of a region is proportional to the volume of the flux tube it is located on. The volume is proportional to $\int \frac{dl}{B}$ and if we approximate our magnetic field as a pure dipole, then B is proportional to $\frac{1}{R^3}$ so the volume is proportional to $\frac{1}{R^4}$. Since $\psi = R \int B \cdot dR$ and again B is proportional to $\frac{1}{R^3}$, this makes ψ proportional to $\frac{1}{R}$. We can calculate the flux, ψ, from the equilibrium code everywhere in space, so we relate the density to ψ as follows: $n = C\psi^{\alpha}$ where C is a constant and $\alpha = 4$ for the case discussed; however, this would be an extremely peaked profile.

Since we know the value of the density and flux a specific point from the probe data, the constant of the equation can be calculated and the density can be determined in all space. In figure 4-4 I have plotted four density profiles along the Z=0 mid-plane with α values of 0, 1, 1.5, and 2. $\alpha = 0$ will give a constant density profile and as α

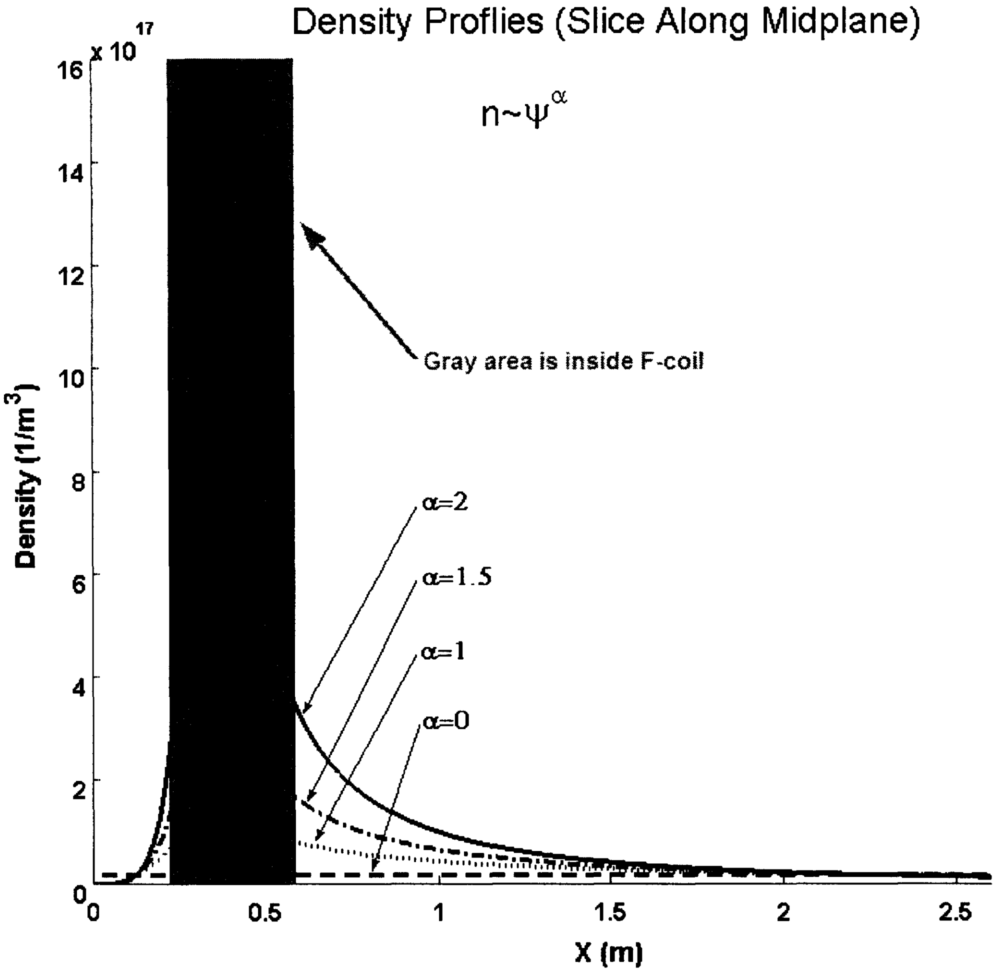

Figure 4-4: Possible density profiles.

is increased, the profile becomes more and more peaked.

The next step is to look at the electron plasma frequency as a function of space along the Z=0 mid-plane. Figure 4-5 also includes the frequencies of the input power, 2.45 GHz and 6.4 GHz, both multiplied by 2π. A cutoff exists where the electron plasma frequency intersects the line representing the input power frequency. For any electron plasma frequency above the input power frequency, the input wave power will not propagate.

For the most peaked profile where $\alpha = 2$, the cutoff for the 2.45 GHz waves is relatively far out in the plasma. As the density profile becomes less peaked this

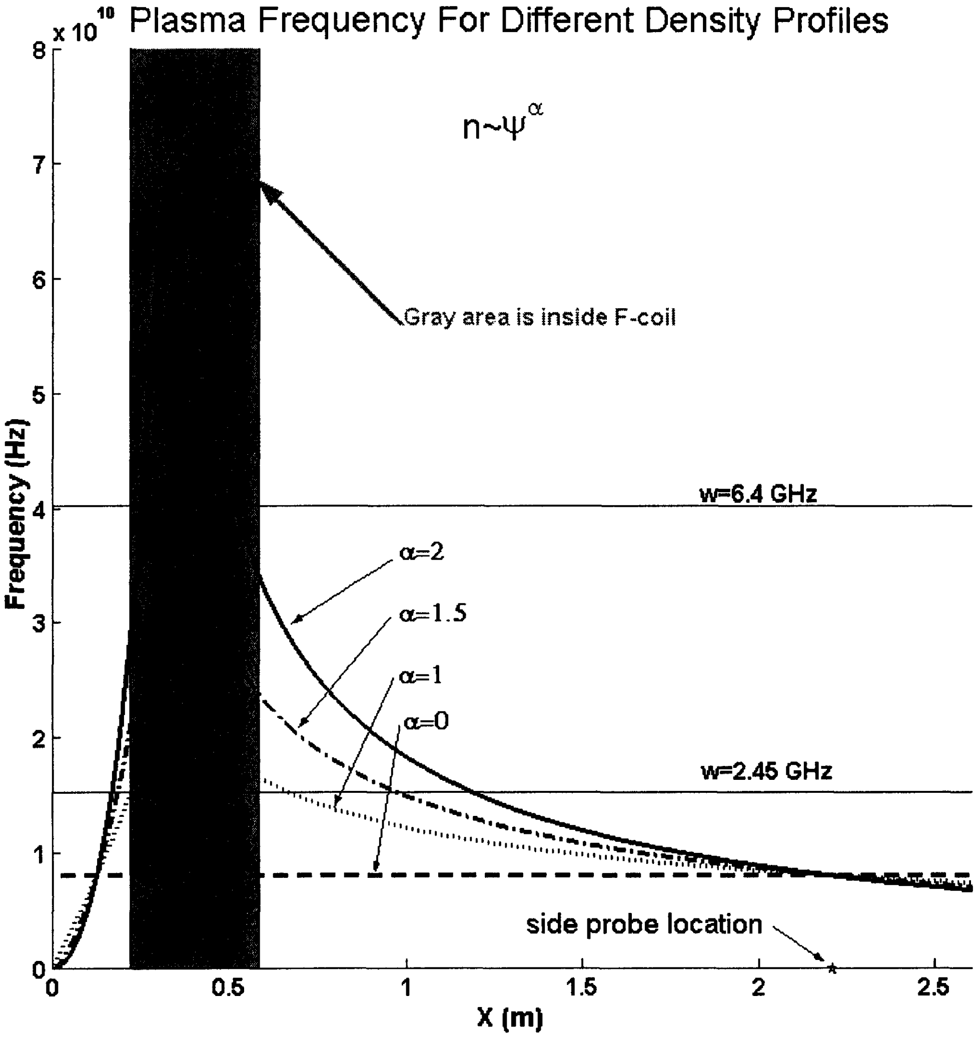

Figure 4-5: Plasma frequency profiles for several density profiles.

density limit moves in towards the coil. For a constant density profile, alpha equals zero, there is no density cutoff, as shown in figure 4-5.

This information can also be plotted as a contour plot where the first harmonic resonances can be seen as well as the fundamental resonances. For values of alpha greater than one the density cutoff extends past the second harmonic, blocking the region where the resonance and the magnetic field are tangent. Not only are the cutoffs sensitive to the density profile, but also to the edge probe measurement. If the density read by the probe decreases by a factor of 2 there is a significant difference

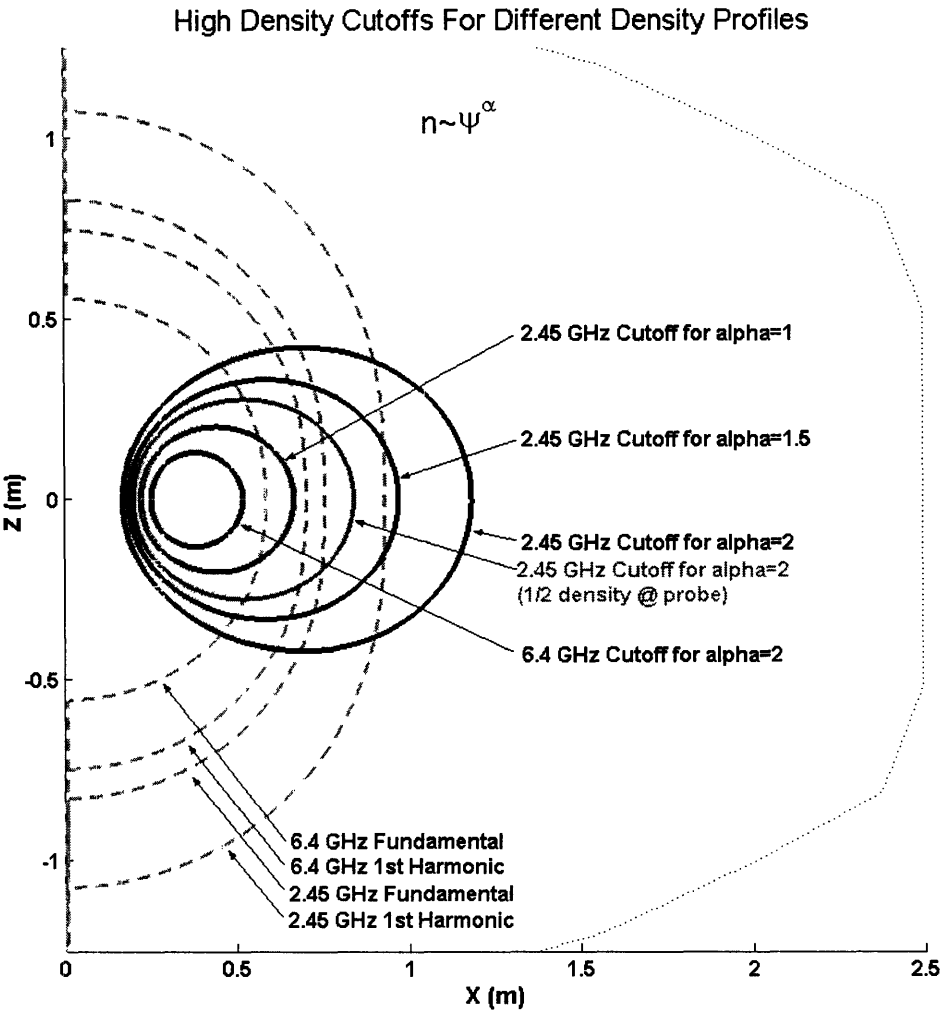

Figure 4-6: High density cutoffs for several density profiles.

in the location of the high density cutoffs. In figure 4-6, the thick grey line is the density cutoffs with one half of the density at the probe as the black line for $\alpha = 2$. Note that there is a 6.4 GHz cutoff in the plasma for only $\alpha = 2$ or higher.

Similar to the affects that the density profile has on the the density cutoff, it also effects the right hand cutoff. The more peaked the density profile is, the further out the right hand cutoff extends as seen in figure 4-7. Also, when one half of the density is used as the density at the probe the right hand cutoff moves back in towards the coil, just like the high density cutoff.

These plots have illustrated the effect of the density profile on the upper hybrid

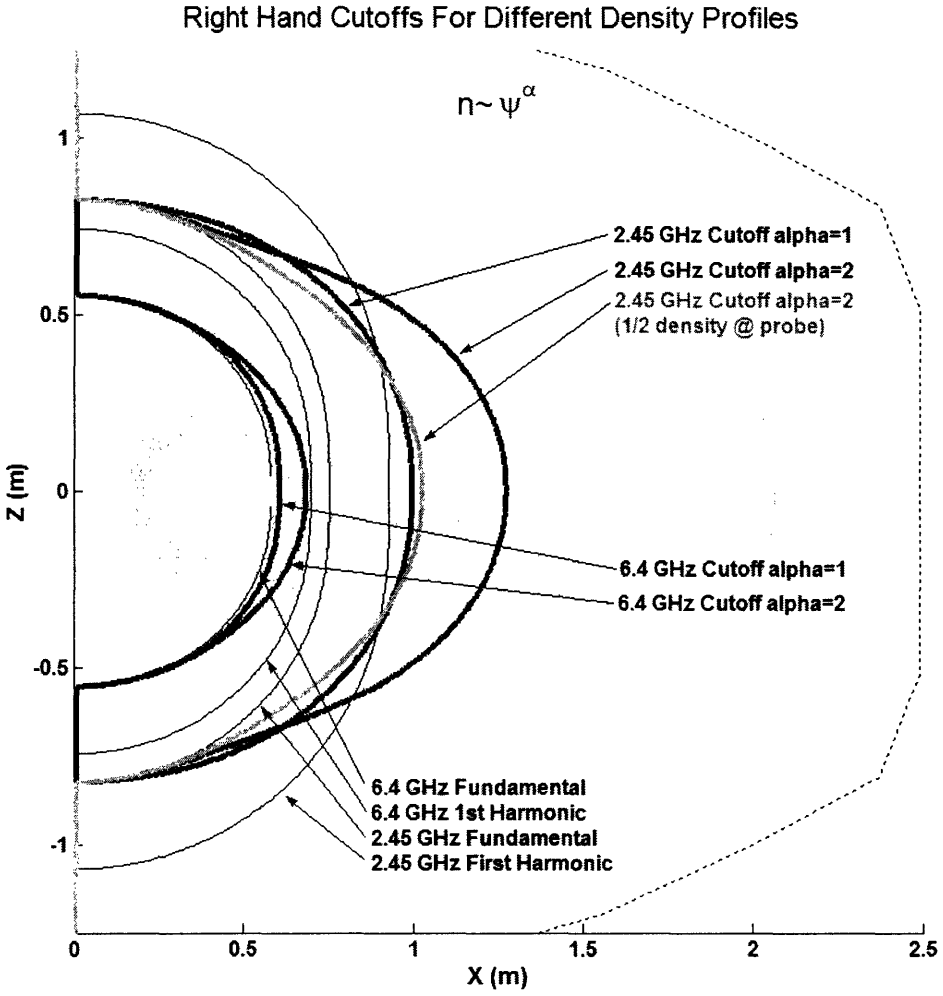

Figure 4-7: Right hand cutoffs for several density profiles.

resonance, the high density cutoff, and the right hand cutoff. For a peaked profile, such as $\alpha = 2$, a large fraction of the 2.45 GHz first harmonic resonance is blocked. By making the density profile less peaked, such as $\alpha = 1$, the right hand cutoff moves back and exposes more of the 2.45 GHz first harmonic resonance. Once we have the diagnostic ability to determine the density profile, we can calculate the resonances and cutoffs and study the accessibility more accurately.

Chapter 5

Power Absorbed Calculations

When plasma is heated by ECRH, the electrons are initially heated at the fundamental resonance, and then are accelerated up to high energies through the first harmonic resonance [18]. Since there are resonances and cutoffs between the fundamental harmonic and where the waves are launched, the waves need to find a way into the fundamental harmonic.

Through ray tracing codes, it has been determined that the waves are only weakly absorbed and that they reflect several times off the vessel walls and F-Coil before they are damped by the plasma [18]. During every reflection off the wall and F-Coil about 50% of the waves come off in O-mode and 50% come off in X-mode, regardless of the incoming wave [19]. The X-mode is cutoff by the right hand cutoff before it gets to the fundamental; however, the O-mode does not get cutoff. Half of the O-mode waves that make it to the F-Coil will be converted to X-mode, which will be strongly absorbed by the fundamental from the high field side [19].

Several attempts to calculate the power absorbed in LDX plasmas have been carried out; however, due to several unknown variables, a quantitative calculation cannot be completed. To calculate the power absorbed at a point in space, many variables must be known including: the magnitude of the magnetic field, the density, the parallel and perpendicular velocities, the electric field from the heating waves, and the values of $k_{\|}$ and $k_{\perp}$ of the heating wave. Since we assume that we are cavity heating, the simple assumption would be that there is an equal distribution of $k_{\|}$

and $k_\perp$ everywhere in the plasma. However, this is not true. Due to the cutoffs there will certain regions where the X-mode heating waves are evanescent. Another difficulty in the calculation of the power absorbed is the lack of a definite density and temperature profile. Since the calculation of the power absorbed is a function of density and temperature, changing the density profile will change not only the locations of the cutoffs, but also the power absorbed profile.

The remainder of this chapter will discuss two different methods of calculating the power absorbed profiles for LDX during shot 50318014. Although these methods cannot produce quantitative profiles of the power absorbed, they both give a qualitative representation of where the power is absorbed in LDX.

5.1 Average Power

The first method of calculating the power absorbed in LDX tries to calculate a most probable power absorbed at every point in space. The power absorbed per unit volume is defined by Stix as [13]:

$$P_\perp = \frac{nZ_s^2 e^2}{m_s|k_\parallel|}|E^-|^2 \int_0^\infty 2\pi v_\perp dv_\perp f\left(v_\perp, v_\parallel^{res}\right) = \frac{nq^2}{m_e|k_\parallel|}|E^-|^2 n_{res} \tag{5.1}$$

where

$$E^- = \frac{E_x - iE_y}{2} \tag{5.2}$$

This definition of E^- comes from the second edition of *Waves in Plasmas.* The older version defines $E^- = E_x - iE_y$, in which case a factor of $\frac{1}{4}$ would be needed in the power absorbed equation.

Also:

$$n_{res} = \int_{-\infty}^{\infty} dv_\parallel \int_0^\infty 2\pi v_\perp dv_\perp f\left(r, v_\perp, v_\parallel^{res}\right) \delta\left(v_\parallel - \frac{\omega - \omega_{ce}}{k_\parallel}\right) \tag{5.3}$$

We assume that the electric field of the heating waves adjusts to a level so that the power absorbed in the plasma is equal to the power input into the vessel. We also assume that we are heating in steady state, and that none of the power is absorbed by the walls of the vessel.

We assume a Maxwellian profile of the form:

$$f\left(r, v_\perp, v_\parallel^{res}\right) = n\sqrt{\frac{m_e}{2\pi T_\parallel}}\left(\frac{m_e}{2\pi T_\perp}\right) e^{-\frac{m_e v_\parallel^2}{2T_\parallel}} e^{-\frac{m_e v_\perp^2}{2T_\perp}} \tag{5.4}$$

After integrating, we get the power absorbed per unit volume:

$$P = \frac{q^2}{m_e}\frac{\pi}{k_\parallel}\sqrt{\frac{m_e}{2\pi T_\parallel}}|E^-|^2 n e^{\left(-\frac{m_e(\omega-\omega_{ce})^2}{2T_\parallel^2 k_\parallel^2}\right)} \tag{5.5}$$

The power absorbed by the first harmonic is also calculated and plotted according to the formula [13]:

$$P_{2\omega} = \left(k_\perp \frac{v_\perp}{\omega_{ce}}\right)^2 \frac{q^2}{m_e}\frac{\pi}{k_\parallel}\sqrt{\frac{m_e}{2\pi T_\parallel}}|E^-|^2 n e^{\left(-\frac{m_e(\omega-2\omega_{ce})^2}{2T_\parallel^2 k_\parallel^2}\right)} \tag{5.6}$$

where the $\left(k_\perp \frac{v_\perp}{\omega_{ce}}\right)^2$ term comes from the Bessel factor $J_o\left(\frac{k_\perp v_\perp}{\omega_{ce}}\right)$, which goes to 1 in the small Larmor radius limit (at the fundamental resonance) but comes into play at the harmonic resonances.

The pressure profile is reconstructed from magnetic measurements, but neither the density profile nor the temperature profile are well measured at this time. The density profile is assumed to have the form $n_e = C\psi^\alpha$, as discussed in section 4.1.3. The constant is calculated using a measurement from the side probe as well as the known flux at that point. The temperature profile is then calculated using $T = \frac{P}{n}$. The pressure, density and temperature profiles on the midplane are show in Fig. 5.1 for $\alpha = 1$. The gap in the profile is the location of the F-Coil.

Another assumption that we make is that $T_\parallel = T_\perp$ which is a possible limit when the coil is levitated. Assuming that we are cavity heating and that there is an equally likely chance that the k-vector will be in any direction, we permit the angle between the k-vector and the magnetic field to vary from 0 to π. Using the Appleton-Hartree form of the dispersion relation, we can calculate n. The Appleton-Hartree form of

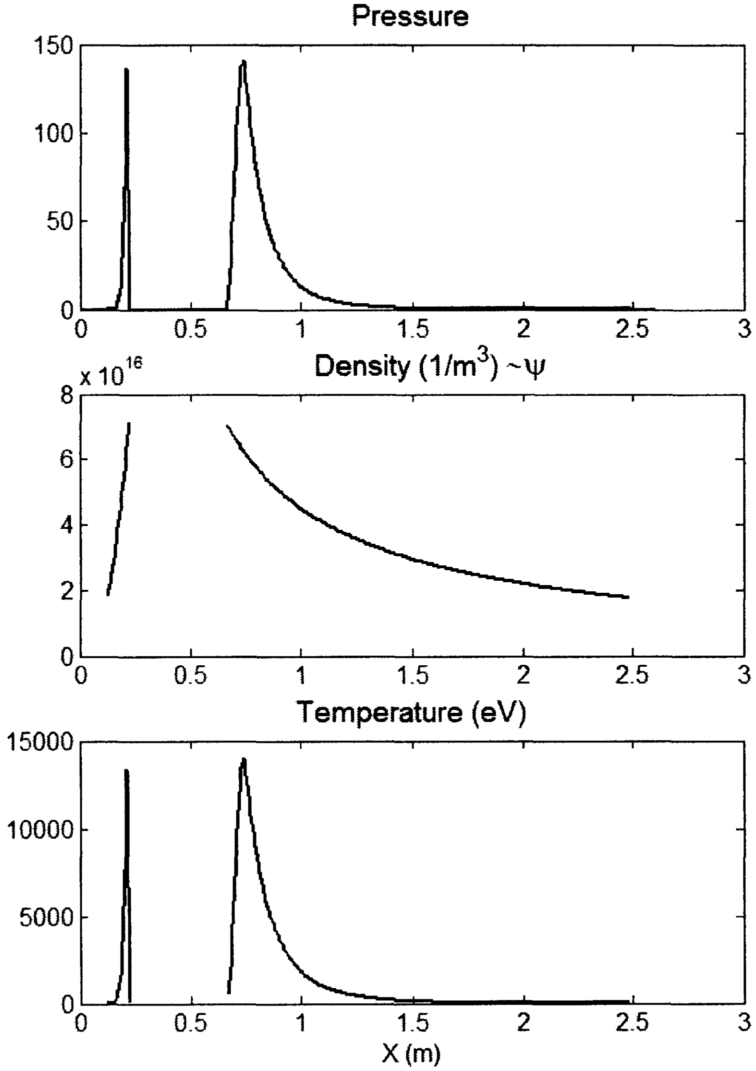

Figure 5-1: Pressure, density, and temperature profiles for $n = C\psi^{\alpha}$.

the dispersion relation is [13]:

$$n^2 = 1 - \frac{2\alpha\omega^2(1-\alpha)}{2\omega^2(1-\alpha) - \omega_{ce}^2 \sin^2\theta \pm \omega_{ce}\Delta} \tag{5.7}$$

where

$$\Delta = \left(\omega_{ce}^2 \sin^2\theta + 4\omega^2 (1-\alpha)^2 \cos^2\theta\right)^{\frac{1}{2}} \tag{5.8}$$

and we ignore the collision terms in

$$\alpha = \frac{\omega_{pe}^2}{\omega(\omega + i\nu)} \Rightarrow \alpha = \frac{\omega_{pe}^2}{\omega^2} \tag{5.9}$$

and

$$\omega_{ce} = \frac{qB}{m_e}\frac{\omega}{\omega + i\nu} \Rightarrow \omega_{ce} = \frac{qB}{m_e}. \tag{5.10}$$

The plus or minus part is for X-mode versus O-mode, so we will use the minus to look at X-mode absorption.

Given a value for n, we calculate $k_{\|} = \frac{n\omega}{c}\cos\theta$, and $k_{\perp} = \frac{n\omega}{c}\sin\theta$ for a number of different thetas ranging from 0 to π for a given point in space. We then plug these values of $k_{\|}$ and $k_{\perp}$ into the power absorbed equation. Due to the geometric effects, a $\sin\theta$ weighting enhances the power absorbed at $\theta = \frac{\pi}{2}$.

The figures generated for the case $n = C\psi$ are shown in figure 5-2. Since this method calculates the most likely value of power absorbed based on all values of $k_{\|}$, which are calculated from the dispersion relation, the cutoff regions are clear. On the high field side of the right hand cutoff there is a region, extending from the first harmonic to the right hand cutoff, where no power is absorbed. In this region, the values of the k-vectors are not real, indicating that the waves evanesce.

The problem with tying to calculate the power absorbed using this method is that we run into numerical problems in the calculations, as seen in figure 5-2. The resonance is almost a delta function, so in order to see the power absorption clearly, a very fine grid around the area of the resonance is needed. Trying to make a fine enough grid to show the characteristics of the resonance is very difficult, so we moved on to a different approach where we would not have to deal with a fine grid.

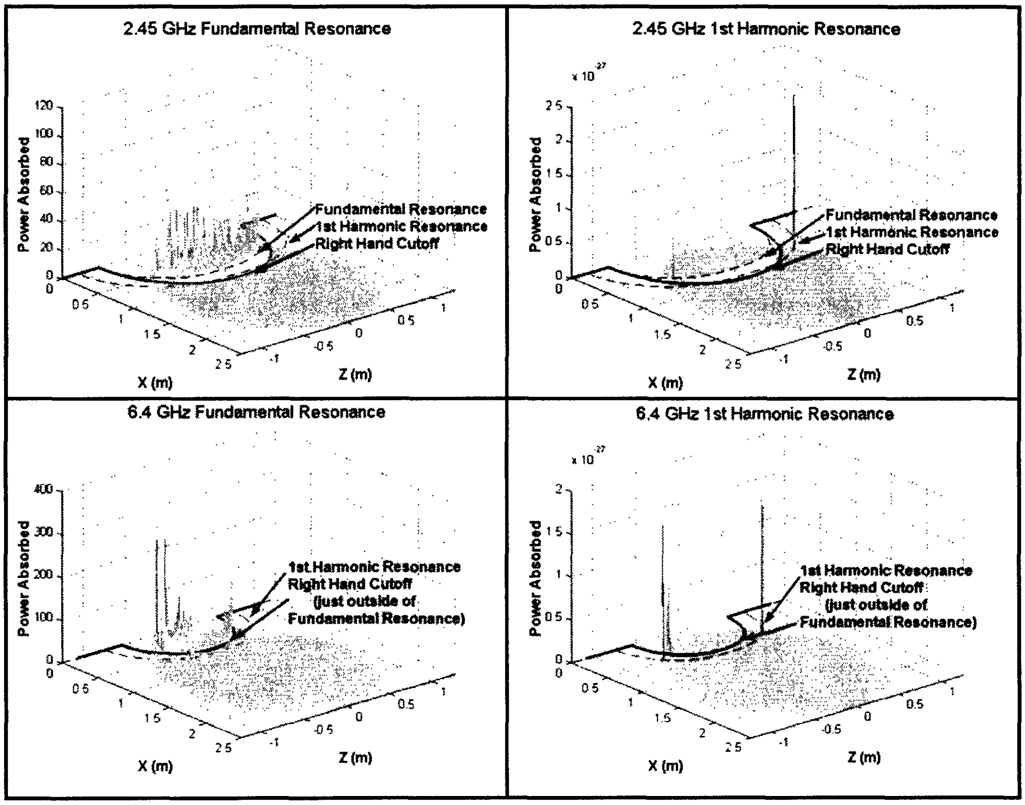

Figure 5-2: Power absorption for a profile where $\alpha = 1$, $(n = C\psi)$.

5.2 Stix's Approximation

The other method of calculating the power absorbed that we looked at makes use of the fact that different $k_{\|}$ interact with different parts of the electron distribution function in the vicinity of and close to the resonant surface. If we integrate over a resonance, the dependence on $k_{\|}$ cancels out of the equation. Stix defines the power absorbed as [13]:

$$P_{\perp} = \frac{nZ_s^2e^2}{m_s|k_{\|}|}|E^{-}|^2 \int_0^{\infty} 2\pi v_{\perp} dv_{\perp} f\left(r, v_{\perp}, v_{\|}^{res}\right) = \frac{nZ_s^2e^2}{m_s|k_{\|}|}|E^{-}|^2 n_{res}\left(r, v_{\|}^{res}\right) \tag{5.11}$$

where

$$n_{res} = \int_{-\infty}^{\infty} dv_{\|} \int_0^{\infty} 2\pi v_{\perp} dv_{\perp} f\left(r, v_{\perp}, v_{\|}^{res}\right) \delta\left(v_{\|} - \frac{\omega - \omega_{ce}}{k_{\|}}\right) \tag{5.12}$$

which simplifies to

$$n_{res} = |k_{\|}| \int_{-\infty}^{\infty} dv_{\|} \int_0^{\infty} 2\pi v_{\perp} dv_{\perp} f\left(r, v_{\perp}, v_{\|}^{res}\right) \delta\left(\omega_{ce} - \omega + k_{\|} v_{\|}\right) \tag{5.13}$$

Changing variables and integrating across the resonance gives:

$$\int_{R1}^{R2} dR n_{res}(r) = n(r) \frac{k_{\|}}{d\omega_{ce}/dR} \tag{5.14}$$

and since $\omega_{ce} = \frac{qB}{m_e}$ this gives:

$$n_{res}(r) = n(r)|k_{\|}| \frac{m_e}{q} \frac{1}{dB/dR} \tag{5.15}$$

Making the power absorbed per unit area on the resonant surface:

$$P_{\perp} = \pi q |E^{-}|^2 n \frac{1}{dB/dR} \tag{5.16}$$

This equation can be used to calculate the power absorbed in a resonance region. Figure 5-3 shows this calculation for the 2.45 GHz fundamental resonance using a

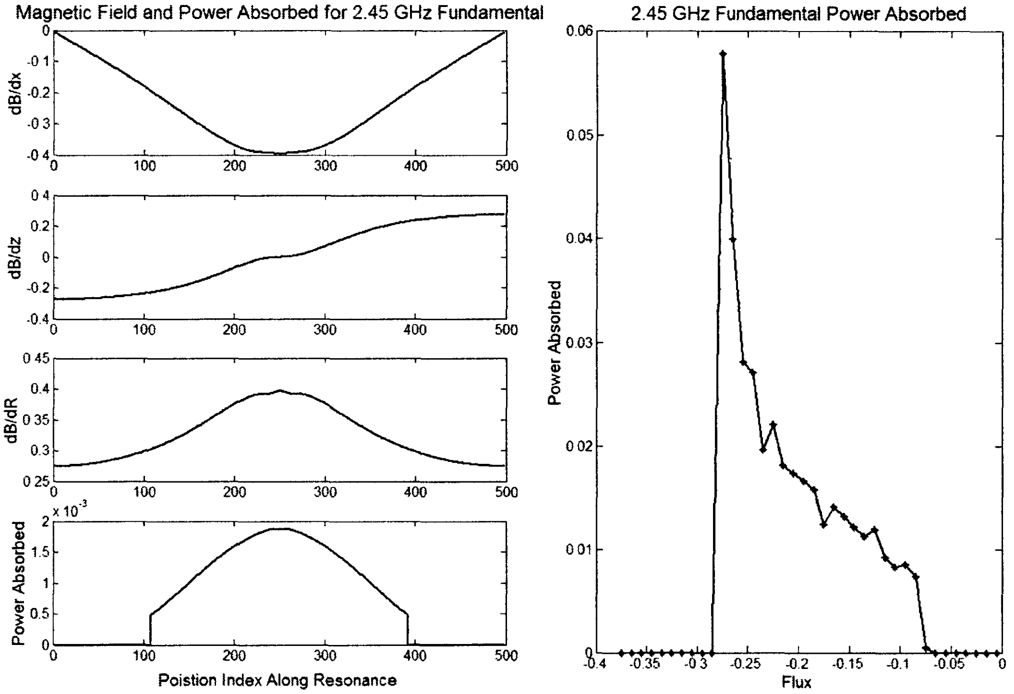

Figure 5-3: Power absorbed (per unit area) calculations using Stix's approximation before being normalized.

density of $n = C\psi$.

Figure 5-3 shows the general distribution shape of power absorbed per flux that we would expect if the resonance were fully accessible.

The next step is to normalize the power absorbed under the assumption that all power input into the vessel is absorbed by the plasma. To do this, the total power absorbed on the 2.45 GHz fundamental is added to the total power absorbed on the 2.45 GHz first harmonic. Assuming that 3000 watts at 2.45 GHz are input into the vessel, the power absorbed per flux plots are normalized. The same process is used to normalize the 6.4 GHz absorption. Plotting the power absorbed per flux on the same figure shows the relative absorption at at different fluxes for different density profiles, as shown in figure 5-4. The 6.4 GHz fundamental absorbs the least total power, since it intersects the coil. Figure 5-4 also shows that for a less peaked profile, such as $\alpha = 0$, the power absorption is spread out over more fluxes. For the more peaked profiles, such as $\alpha = 2$, more power is absorbed locally at a given flux surface.

This information can also be viewed in a plot of $\frac{d(Power)}{d(Volume)}$ plotted vs. $X(m)$, as in figure 5-5. This figure is heavily weighted because of the small volumes of the flux loops near the F-coil where most of the absorption takes place.

For each resonance, the flux tube with the maximum power absorption can be found and contour plotted on top of a plot of the resonances. For $n = C\psi$, the most power absorbed on the 6.4 GHz fundamental is at $\psi = -0.2950$. Similarly, the first harmonic resonance for the 6.4 GHz source also absorbs the most power at$\psi = -0.2950$. The 2.45 GHz fundamental and first harmonic absorb the most power at $\psi = -0.2750$ and $\psi = -0.2150$ respectively. Figure 5-6 illustrates that the flux tubes that absorb the most power are the ones that are tangent to the resonant surfaces at the mid-plane.

Although this method avoids the problem of calculating the correct value of $k_{\|}$, it has limitations. The Stix method assumes that absorption only occurs in a very narrow region around the resonance. Resonance regions, however, have a finite width, which is dependent on the magnetic field, density, and temperature profiles. Another weakness of this method is that it assumes that the resonances are fully accessible. For the density profile plotted, we know that part of the 2.45 GHz first harmonic is cutoff by the right hand cutoff, whereas this method calculates that the most power is absorbed in the flux tube tangent to the resonance on the mid-plane (which is in the evanescent region of the right hand cutoff).

In order to do a quantitative calculation of the power absorbed, the density and temperature profiles must be known. Furthermore, ray tracing codes must be developed to determine more accurately the values of $k_{\|}$ and $k_{\perp}$ at every point in the plasma.

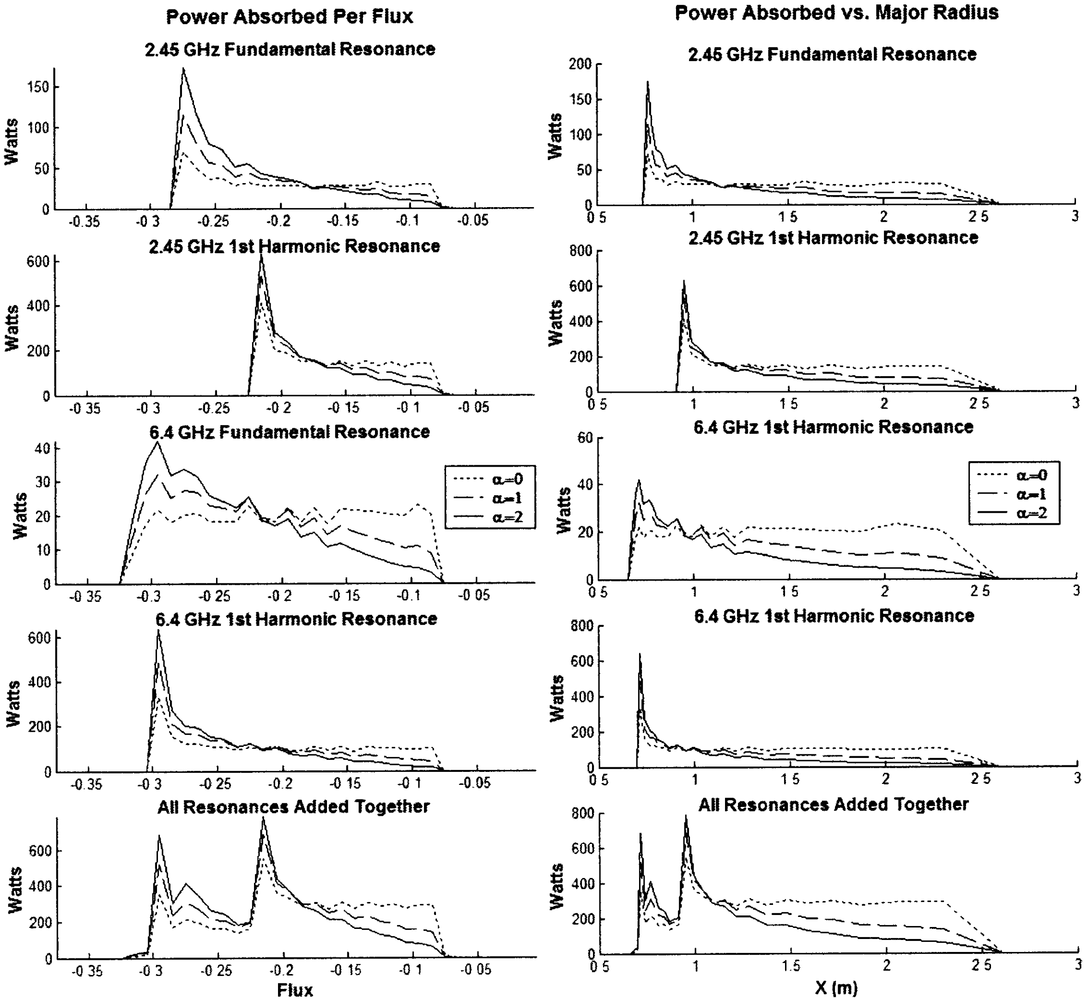

Figure 5-4: Power absorbed per flux loop (left) and vs major radius (right) for $n = C\psi^{\alpha}$ calculated using Stix's approximation. Data is plotted for $\alpha = 0$, $\alpha = 1$, and $\alpha = 2$.

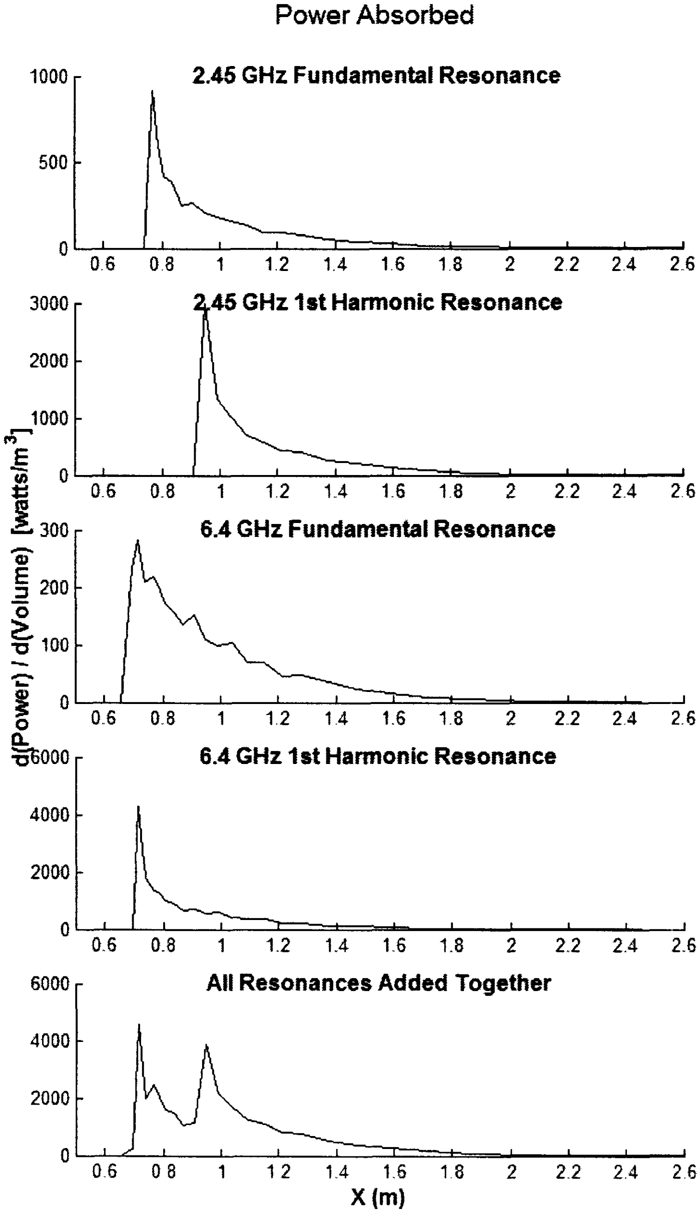

Figure 5-5: $\frac{d(Power)}{d(Volume)}$ plotted vs. $X(m)$ calculated using Stix's approximation. Data is plotted for $\alpha = 1$ ($n = C\psi$).

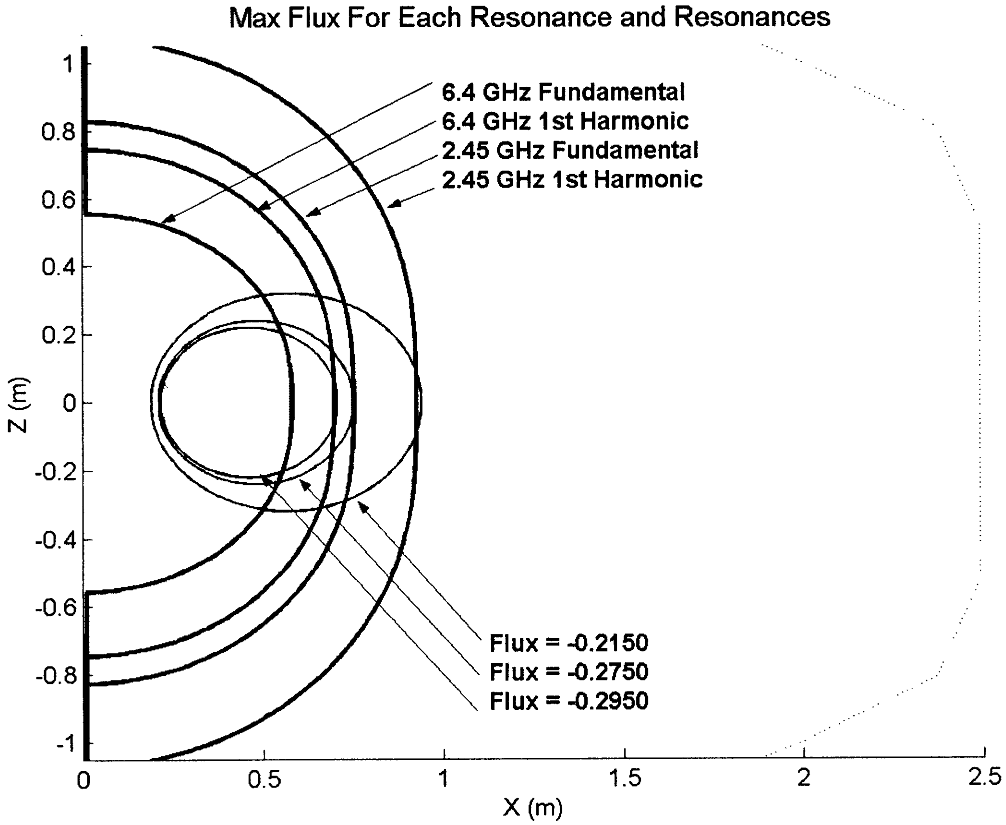

Figure 5-6: Locations of flux loops with maximum absorption for $\alpha = 1$, $(n = C\psi)$.

Chapter 6

Conclusion

Electron cyclotron resonance heating is a relatively simple system to setup; however, it is a difficult system to simulate. A cavity heating system has added complexities that a directional system does not encounter. We have successfully implemented a 2.45 GHz and a 6.4 GHz system which provide the ECRH heating for LDX plasmas. Calculations of power absorption need detailed information about the direction and magnitude of the k-vector which is complicated in any cavity heating system.

Other variables such as the density and temperature are also required to calculate the power absorption. These parameters are normally well known for most reactors, and soon will be known for LDX. Not knowing the exact profiles makes it impossible to calculate the precise locations of the cutoffs and resonances other than the fundamental resonance and its harmonics. By assuming general profile shapes these locations can be estimated; however, once the exact profiles are known, the locations can be more accurately determined using the same methods used in this thesis.

In the near future, several more interferometer chords will be added, which will help determine the density profile. Adding 10 kW from the 10.5 GHz source will also help to develop the calculations of the profiles. Being able to add another 10 kW of power at another location will change the profiles. These changes in profiles will be picked up by the new interferometer chords, allowing a more exact calculation of the profiles. This will, in turn, lead to more accurate calculations of the power absorption in the Levitated Dipole Experiment.

Bibliography

[1] J. Kesner, L. Bromberg, M. Mauel, D. T. Garnier, and J.M. Dawson. *The Dipole Fusion Confinement Concept: A White Paper for the Fusion Community.* MIT Plasma Science and Fusion Center (PSFC/RR-98-5), 1998.

[2] A. Hasegawa. *A Dipole Field Fusion Reactor.* Plasma Physics & Controlled Fusion (11(3):147), 1987.

[3] J. Kesner, D. T. Garnier, A. Hansen, and M. E. Mauel. *Stability of a Levitated Dipole Confined Plasma in Closed Line Magnetic Fields.* Presented at 44th Annual Meeting of the APS Division of Plasma Physics (KP1.118), November 13, 2002.

[4] J. Kesnser, D.T. Garnier, A. Hansen, M. Mauel, and L. Bromberg. *Helium Catalyzed D-D Fusion in a Levitated Dipole.* Nuclear Fusion Vol. 44, 2004.

[5] D.T. Garnier, J. Kesner, and M. Mauel. *ECRH in the Levitated Dipole Experiment.* Presented at 13th Topical Conference on Applications of Radio Frequency Power to Plasmas, 1999.

[6] D.T. Garnier, J. Kesner, and M. Mauel. *Magnetohydrodynamic Stability in a Levitated Dipole.* Physics of Plasmas Vol. 6, 1999.

[7] A.K. Hansen, S. Mahar, A.C. Boxer, J.L. Ellsworth, D.T. Garnier, I. Karim, J. Kesner, M. Mauel, and E.E. Ortiz. *Initial Results of Multi-Frequency Electron Cyclotron Frequency Heating in the Levitated Dipole Experiment.* 16th Topical Conference on Radiofrequency Power in Plasmas, 2005.

[8] J. Wesson. *Tokamaks.* Oxford University Press, 2004.

[9] J. Kesner, L. Bromberg, D. T. Garnier, and M. Mauel. *Plasma Confinement in a Levitated Dipole.* Presented at 17th IAEA Conference of Plasma Physics and Controlled Nuclear, 1998.

[10] A. Hansen, D. Garnier, J. Kesner, M. Mauel, and A. Ram. *ECRH in the Levitated Dipole Experiment.* AIP Conference Proceedings (14th Topical Conference on Radio Frequency Power in Plasmas), 2001.

[11] D. T. Garnier, A.K. Hansen, M.E. Mauel, E.E. Ortiz, A. Boxer, J. Ellsworth, O. Grulke, I. Karim, J. Kesner, J. Minervini, P. Michael, and A. Zhukovsky. *Overview and Experimental Program of the Levitated Dipole Experiment.* Presented at APS Plasma Physics Meeting, 2003.

[12] J. Ellsworth. *X-Ray Diagnostics for the Levitated Dipole Experiment.* Masters Thesis, Massachusetts Institute of Technology, 2004.

[13] T.H. Stix. *Waves in Plasmas.* American Institute of Physics, 1992.

[14] D.T. Garnier, J. Kesnser, M. Mauel. *Magnetohydrodynamic Stability In a Levitated Dipole.* Physics of Plasmas, 1999.

[15] H.P. Warren and M.E. Mauel. *Observations of Chaotic Particle Transport Driven by Drift-Resonant Fluctuations in the Collisionless Terrella Experiment.* Physics of Plasmas, 1995.

[16] Y. Ogawa. *Levitated Superconductor Ring Trap (Mini-RT) Project.* IAEA Confrence Session (IC/P-12), 2003.

[17] D.T. Garnier *First Plasma Results on the Levitated Dipole Experiment.* MIT Plasma Science and Fusion Center Plasma Seminar, 2005.

[18] J. Kesner. *High Beta Plasmas Confined in a Dipole.* Paper to be published.

[19] D. Bachelor. *Detailed Modeling of Microwave Energy Deposition in EBT Devices.* Nuclear Fusion, Vol. 21, 1983.